CAPITAL UNIVERSITY OF SCIENCE AND TECHNOLOGY, ISLAMABAD

Numerical Investigation of Radiative Magneto-Micropolar Flow and Heat Transfer in a Channel with Dual Cylinders

by

Muhammad Bilal

A thesis submitted in partial fulfillment for the degree of Master of Philosophy

in the

Faculty of Computing
Department of Mathematics

2026

Copyright © 2026 by Muhammad Bilal

All rights reserved. No part of this thesis may be reproduced, distributed, or transmitted in any form or by any means, including photocopying, recording, or other electronic or mechanical methods, by any information storage and retrieval system without the prior written permission of the author.

CERTIFICATE OF APPROVAL

Numerical Investigation of Radiative Magneto-Micropolar Flow and Heat Transfer in a Channel with Dual Cylinders

by

Muhammad Bilal

(Registration No: MMT241005)

THESIS EXAMINING COMMITTEE

S. No.	Examiner	Name	Organization
(a)	External Examiner	Dr. Muhammad Shakeel	UOW, Wah Cantt
(b)	Internal Examiner	Dr. Abid Kamran	CUST, Islamabad

Dr. Muhammad Sabeel Khan
Thesis Supervisor
March, 2026

Dr. Muhammad Sagheer
Head
Dept. of Mathematics
March, 2026

Dr. Muhammad Abdul Qadir
Dean
Faculty of Computing
March, 2026

Author's Declaration

I, **Muhammad Bilal** hereby state that my MPhil thesis titled "**Numerical Investigation of Radiative Magneto-Micropolar Flow and Heat Transfer in a Channel with Dual Cylinders**" is my own work and has not been submitted previously by me for taking any degree from Capital University of Science and Technology, Islamabad or anywhere else in the country/abroad.

At any time if my statement is found to be incorrect even after my graduation, the University has the right to withdraw my MPhil Degree.

(Muhammad Bilal)

Registration No: MMT241005

Plagiarism Undertaking

I solemnly declare that research work presented in this thesis titled "**Numerical Investigation of Radiative Magneto-Micropolar Flow and Heat Transfer in a Channel with Dual Cylinders**" is solely my research work with no significant contribution from any other person. Small contribution/help wherever taken has been duly acknowledged and that complete thesis has been written by me.

I understand the zero tolerance policy of the HEC and Capital University of Science and Technology towards plagiarism. Therefore, I as an author of the above titled thesis declare that no portion of my thesis has been plagiarized and any material used as reference is properly referred/cited.

I undertake that if I am found guilty of any formal plagiarism in the above titled thesis even after award of MPhil Degree, the University reserves the right to withdraw/revoke my MPhil degree and that HEC and the University have the right to publish my name on the HEC/University website on which names of students are placed who submitted plagiarized work.

(Muhammad Bilal)

Registration No: MMT241005

Acknowledgement

First and foremost, all praises and thanks are due to **Allah Almighty**, the Most Merciful and Compassionate, who bestowed upon me the strength, wisdom, and perseverance to complete this research work. His infinite blessings and guidance have been the source of light throughout this academic journey. I send my sincerest blessings and peace upon the **Holy Prophet Muhammad (PBUH)**, the ultimate source of knowledge and guidance for all humanity, whose teachings continue to inspire the pursuit of knowledge and excellence.

I would like to express my deepest gratitude and appreciation to my family for their unwavering support, prayers, and encouragement throughout my academic pursuits. To my beloved **parents**, whose sacrifices, prayers, and unconditional love have been my foundation and strength, this achievement is as much yours as it is mine. Your constant faith in me has been my driving force during challenging times. I am profoundly grateful to my thesis supervisor, **Dr. Muhammad Sabeel Khan**, for his invaluable guidance, continuous support, and expert supervision throughout this research. His profound knowledge, insightful suggestions, and patience have been instrumental in shaping this work. My sincere thanks to the faculty members of the **Department of Mathematics**, Capital University of Science and Technology, for their quality education and support during my MPhil program. Special thanks to **Dr. Muhammad Sagheer**, Head of Department of Mathematics, for providing excellent research facilities and academic environment.

I extend my appreciation to my teachers throughout my academic journey, from early education to university level, who instilled in me the love for learning and provided the foundation upon which this work is built.

(Muhammad Bilal)
Registration No: MMT241005

Abstract

This research presents a comprehensive numerical investigation of radiative magneto Micropolar flow and heat transfer in a channel containing dual cylinders arranged in tandem configuration. The study addresses the complex multiphysics coupling between Eringen's micropolar fluid theory, magnetohydrodynamics, and thermal radiation effects, which remains largely unexplored in existing literature despite its significant practical applications in heat exchangers, microfluidic devices, and thermal management systems. The mathematical formulation incorporates the complete set of governing equations for mass, linear momentum, angular momentum, and energy conservation, with thermal radiation modeled using the Rosseland approximation for optically thick media. The weak formulation employs Taylor-Hood (P_2-P_1) elements for velocity-pressure coupling and P_2 elements for microrotation and temperature fields. A computational framework is developed using the finite element method based on the weak formulation. The results are validated against the established Turek and Schafer benchmark case for flow around a circular cylinder. Systematic parametric study is carried out to analyze the individual and combined effects of dimensionless parameters including Reynolds number (Re), micropolar coupling parameter (K), Eringen number (Er), Prandtl number (Pr), Eckert number (Ec), radiation parameter (Rd), magnetic parameters (α, β, M_s), and magnetization dissipation parameter (Γ). The obtained results reveal that increasing Reynolds number enhances flow separation, intensifies microrotation activity, and improves convective heat transfer. The micropolar coupling parameter significantly influences the interaction between translational and rotational motion with higher K values, strengthening this coupling and altering re-circulation patterns. Magnetic fields effectively suppress vortex shedding and modify wake dynamics, while thermal radiation substantially elevates temperature levels throughout the domain. The research identifies optimal parameter ranges for thermal-hydraulic performance enhancement and establishes correlations between dimensionless parameters and performance metrics.

Contents

List of Figures

List of Tables

Abbreviations

BC	Boundary Condition
CFD	Computational Fluid Dynamics
Ec	Eckert Number
Er	Eringen Number
FEM	Finite Element Method
IC	Initial Condition
MHD	Magnetohydrodynamics
MMR	Magneto-Microrotational
PDE	Partial Differential Equation
Pr	Prandtl Number
Rd	Radiation Parameter
Re	Reynolds Number
2D	Two-Dimensional

Symbols

D	Cylinder diameter (characteristic length)
H	Channel height
L	Channel length
d_{AB}	Distance between cylinder centers
u, v	Dimensional velocity components
U, V	Dimensionless velocity components
p, P	Pressure (dimensional and dimensionless)
ψ	Stream function
w, W	Microrotation velocity (dimensional and dimensionless)
j	Micro-inertia density
η	Dynamic (Newtonian) viscosity
η_r	Microrotational viscosity
γ	Spin-gradient viscosity
ρ	Density
ν	Kinematic viscosity
T	Temperature
θ	Dimensionless temperature
κ	Thermal conductivity
c_p	Specific heat at constant pressure
B_0	Magnetic field intensity
H_0	Applied magnetic field intensity
M_0	Equilibrium magnetization
σ	Electrical conductivity
τ	Magnetic relaxation time
t	Time

α, β	Magnetic coupling parameters
Γ	Magnetization dissipation parameter
K	Micropolar coupling parameter
K_m	Spin gradient viscosity parameter
Re	Reynolds number
Pr	Prandtl number
Ec	Eckert number
Er	Eringen number
Rd	Radiation parameter
M_s	Magnetic parameter
Ω	Flow domain
$\partial\Omega$	Domain boundary
$\mathbf{n}$	Unit normal vector

Chapter 1

Introduction

1.1 Background and Motivation

The study of fluid flow past cylindrical structures is a fundamental problem in fluid mechanics, critical to applications ranging from heat exchangers and nuclear reactor design to offshore engineering and microfluidic systems. The interaction of a fluid with solid obstacles generates complex phenomena such as vortex shedding, wake instabilities, and unsteady hydrodynamic forces, which are central to understanding flow-induced vibrations and optimizing system performance [1].

Classical Newtonian fluid models, while successful for simple fluids, are often inadequate for describing the behavior of complex fluids with internal microstructures, such as polymeric solutions, liquid crystals, colloidal suspensions, and blood. To address this limitation, Eringen introduced the theory [2] of micropolar fluids. This framework extends the classical Navier-Stokes equations by introducing independent rotational degrees of freedom for fluid particles, thereby accounting for microrotation and couple stresses. This provides a more physically realistic model for fluids where the microstructure significantly influences the macroscopic transport of momentum and energy [3]. The integration of magnetohydrodynamics (MHD) with micropolar theory creates a powerful multiphysics framework.

The application of a magnetic field to an electrically conducting micropolar fluid

induces Lorentz forces that interact with both the linear velocity and microrotational fields. This interplay offers a potent mechanism for active flow control and stabilization, with relevance to areas including materials processing, electromagnetic pumping, and biomedical systems [4, 5]. The flow around multiple cylinders in a confined channel introduces a higher level of complexity due to wake interference effects. The wake generated by an upstream cylinder dramatically alters the flow field experienced by a downstream cylinder, significantly affecting the hydrodynamic forces on both. This tandem configuration is ubiquitous in engineering systems, such as tube bundles in heat exchangers and arrays of nuclear fuel rods [6, 7].

Despite extensive research in these individual areas, a significant gap exists in the systematic investigation of how micropolar parameters, particularly the Eringen number (Er), govern the transition in flow regimes and control the drag and lift force dynamics in a magneto-micropolar fluid flow past multiple confined cylinders. This thesis addresses this gap by focusing on the novel role of the Eringen number in stabilizing the flow and suppressing force oscillations, providing new benchmarks for the design of advanced thermal-fluid systems.

1.2 Literature Review

The theoretical foundations of micropolar fluids were established by Eringen [2], who introduced the concept of fluids with microstructures possessing independent rotational degrees of freedom. This groundbreaking work was expanded in subsequent texts [3, 8], which detailed the mathematical formalism and applications of the theory. Ariman et al. [9] provided a comprehensive early review, highlighting the model's utility for complex fluids. The applicability of micropolar theory has been demonstrated across various flow configurations. Rees and Bassom analyzed the classic Blasius boundary layer problem for a micropolar fluid [10], revealing fundamental modifications to the velocity and microrotation profiles. The theory has also proven valuable in microfluidic contexts. Papautsky et al. experimentally

demonstrated that micropolar fluid theory more accurately predicts flow behavior in microchannels compared to the Newtonian model [11].

The investigation of micropolar fluids under magnetic fields has garnered significant interest. Mohamad and Abo-Dahab [12] studied MHD free convection flows, incorporating effects of variable viscosity, thermal radiation, and chemical reaction. Shit and Roy [13] provided a detailed analysis of transient MHD flow and heat transfer in a channel, revealing the complex temporal development of the microrotation field. More recently, Khan et al. [14] developed a robust finite element framework in FreeFEM++ for simulating magneto-micropolar flows, a methodology that strongly informs the present work.

Magnetohydrodynamics, since its inception by Alfven [15], has evolved into a critical tool for flow control. Foundational textbooks by Sutton [4] and Moreau [5] detail the principles and engineering applications of MHD. The effect of magnetic fields on flows past obstacles is main area of research. Chatterjee and Gupta [16] numerically investigated MHD flow and heat transfer behind a square cylinder in a duct, demonstrating strong suppression of vortex shedding under a high magnetic field. Maurya et al. [17] analyzed transient MHD flow in a circular cylinder, highlighting the damping effect of the magnetic field on flow oscillations. These studies establish the role of magnetic parameters as effective tools for stabilizing wakes and modifying force coefficients.

The flow around multiple cylinders is a classic problem due to its practical importance and complex fluid dynamics. Zdravkovich [1] provided an exhaustive review of flow patterns and interference effects for various cylinder arrangements. The pioneering experimental work of Igarashi [6, 7] on two cylinders in tandem meticulously categorized flow regimes based on spacing, identifying critical transitions from single-body behavior to independent vortex shedding. Numerical studies have further elucidated these complex interactions. Carmo and Meneghini [18] performed a detailed numerical investigation of tandem cylinders, providing insights into the bifurcations in the flow field. Recent studies continue to explore

this configuration; Ali et al. [19] compared the thermal and hydrodynamic behavior of tandem, staggered, and side-by-side cylinders, while Duong at el. [20] investigated the complex dynamics of flows past three inclined elliptic cylinders. The benchmark work of Turek and Schafer [21] remains a critical standard for validating numerical methods for cylinder flows.

The computational analysis of coupled multiphysics flows, such as magneto micropolar fluids, demands robust numerical techniques. The finite element method (FEM) is particularly well-suited for this task due to its ability to handle complex geometries and coupled systems. The text by Reddy [22] provides a comprehensive foundation for FEM, while the work of Hecth [23] on FreeFEM++ has made it a powerful and accessible tool for the computational fluid dynamics community. The application of FreeFEM++ to micropolar and MHD flows is exemplified by the work of Khan et al. [14], who implemented a direct and iterative finite element approach for magneto-micropolar channel flow. The use of stable finite element pairs, such as the Taylor-Hood (P2-P1) elements, is crucial for obtaining accurate and stable solutions for incompressible flows.

1.3 Research Gaps and Contributions

Despite extensive research in the individual areas of micropolar fluids, magnetohydrodynamics, thermal radiation, and flow around multiple cylinders, significant knowledge gaps remain in understanding the coupled effects of these phenomena. The comprehensive literature review reveals several important limitations in the existing research:

First, most studies on micropolar fluids have focused on simple geometries or single obstacles, with limited attention to complex configurations involving multiple cylinders in confined channels. The interaction between microrotational effects and wake interference in tandem cylinder arrangements remains poorly understood, particularly in the presence of magnetic fields and thermal radiation.

Second, while MHD effects have been extensively studied for Newtonian fluids, their interaction with micropolar fluids in complex geometries requires further investigation. The combined effects of magnetic fields on both translational and rotational degrees of freedom in multi-cylinder configurations represent an underexplored research area with significant practical implications.

Third, the incorporation of thermal radiation effects into magneto-micropolar flow analyses has been relatively limited, particularly for channel flows with multiple immersed bodies. The complex interplay between radiative heat transfer, magnetic fields, and microrotational effects necessitates comprehensive numerical investigation to establish design guidelines for thermal management systems.

Fourth, validated computational frameworks for simulating coupled radiative magneto micropolar flows are scarce in the literature. The development and validation of such frameworks against established benchmarks is essential for reliable prediction of complex flow and heat transfer phenomena in engineering applications.

Fifth, systematic parametric studies examining the combined effects of Eringen's micropolar parameters, magnetic parameters, and radiation parameters on flow characteristics and heat transfer performance are lacking. Such studies are necessary for identifying optimal parameter ranges and establishing design correlations for practical applications.

This research aims to address these knowledge gaps by conducting a comprehensive numerical investigation of radiative magneto-micropolar flow and heat transfer in a channel with dual cylinders in tandem arrangement. The study systematically examines the effects of Eringen's micropolar parameters and magnetic parameters on flow characteristics, thermal performance, and heat transfer enhancement, with particular emphasis on:

i) The development and validation of a robust computational framework for coupled radiative magneto-micropolar flows

ii) Detailed analysis of wake interference and vortex dynamics in the presence of microrotational and magnetic effects

iii) Quantification of heat transfer enhancement through combined radiation, magnetic field, and micropolar effects

The findings of this research are expected to contribute significantly to the fundamental understanding of complex multiphysics flows and provide practical insights for designing advanced thermal management systems in various engineering applications.

1.4 Thesis Organization

This thesis is organized into five chapters, each addressing specific aspects of the research:

Chapter 2 presents theoretical foundations and preliminary concepts essential for understanding micropolar fluid theory, magnetohydrodynamics, thermal radiation, and numerical methods. This chapter establishes mathematical framework upon which subsequent analysis is built.

Chapter 3 details reproduction and validation of Turek and Schäfer benchmark case (Benchmark 2D-2), establishing credibility of numerical methodology employed in this research. The chapter includes comprehensive validation against established results for flow around circular cylinder.

Chapter 4 presents main numerical investigation of radiative magneto-micropolar flow and heat transfer in channel with dual cylinders. This chapter includes detailed mathematical modeling, numerical implementation, parametric study design, and comprehensive analysis of results.

Chapter 5 summarizes principal findings, draws conclusions based on research objectives and suggests directions for future research.

The thesis concludes with references and appendices containing supplementary information, including detailed parameter ranges, mesh specifications, and additional results supporting main findings presented in the chapters.

Chapter 2

Preliminaries and Theoretical Foundations

This chapter presents the fundamental concepts and theoretical frameworks essential for understanding the mathematical modeling and numerical simulation of radiative magneto-micropolar flow and heat transfer. The chapter begins with an overview of continuum mechanics fundamentals, including the continuum hypothesis and conservation laws that form the basis of fluid dynamics. Following this, the theory of micropolar fluids is introduced, with particular emphasis on Eringen's pioneering work that extends classical Newtonian fluid mechanics to account for microstructural effects. The governing equations for micropolar fluids, including conservation of mass, linear momentum, and angular momentum, are derived and discussed in detail. The constitutive equations and physical interpretation of key micropolar parameters, such as the micropolar coupling parameter K and the Eringen number Er, are provided to establish a clear understanding of their significance in the present study.

The chapter also covers the fundamental principles of magnetohydrodynamics (MHD), including Maxwell's equations, Ohm's law for moving media, and the Lorentz force, which are essential for modeling the interaction between the electrically conducting micropolar fluid and the applied magnetic field.

Additionally, the basics of thermal radiation and the Rosseland approximation for optically thick media are presented, as radiative heat transfer plays a crucial role in the energy equation. Finally, an introduction to the finite element method is provided, which serves as the numerical framework for solving the coupled partial differential equations governing the flow and heat transfer phenomena. This theoretical foundation establishes the necessary background for the subsequent chapters, where the numerical methodology is validated and applied to the dual-cylinder configuration.

2.1 Continuum Mechanics Fundamentals

This section provides an overview of essential continuum mechanics concepts required for understanding fluid behavior.

2.1.1 Continuum Hypothesis

The continuum hypothesis forms the foundational assumption of classical fluid mechanics, postulating that matter is continuously distributed throughout space without discrete molecular structure. This approximation remains valid when the characteristic length scale of the flow is much larger than the mean free path of the molecules . For a fluid containing micro-elements, this hypothesis requires careful consideration, particularly when dealing with micropolar fluids where the microstructural effects become significant at smaller scales [24].

The fundamental assumption states that at any point $\mathbf{x}$ in the flow domain and at any time t, there exists an elementary volume δV that is sufficiently large to contain a statistically significant number of molecules, yet small enough compared to the characteristic length scale of the flow. This allows the definition of field quantities such as density $\rho(\mathbf{x}, t)$, velocity $\mathbf{u}(\mathbf{x}, t)$, and temperature $T(\mathbf{x}, t)$ as continuous functions of space and time.

Mathematically, the continuum hypothesis enables the definition of density at a point as:

$$\rho(\mathbf{x}, t) = \lim_{\delta V \to \delta V^*} \frac{\delta m}{\delta V}, \tag{2.1}$$

where δV^* represents the smallest volume over which the statistical average remains meaningful, typically containing 10^6 to 10^9 molecules for most engineering applications [25].

2.1.2 Differential and Integral Approaches in Fluid Mechanics

In fluid mechanics, two complementary approaches are used to describe the behavior of a continuum: the differential approach and the integral approach [27]. Both are essential for deriving and applying the governing equations.

2.1.2.1 Differential Approach

The differential approach aims to calculate the flow properties at *every point* in a given flow field in the form $P(x, y, z, t)$, $\mathbf{u}(x, y, z, t)$, etc. [27]. From this detailed knowledge of the flow field, overall features can be deduced. However, solving the differential equations of motion for complex geometries is computationally expensive and typically requires numerical methods such as computational fluid dynamics (CFD).

2.1.2.2 Integral Approach

The integral approach considers a finite *control volume* encompassing the region of interest. Instead of seeking pointwise information, it calculates the overall or global features by studying the net fluxes of mass, momentum, and energy [27].

2.1.2.3 Reynolds Transport Theorem

The Reynolds Transport Theorem is the fundamental tool that connects the rate of change of an extensive property of a system to the rate of change within a control volume and the flux across its boundaries. For a fixed control volume Ω with boundary $\partial\Omega$, the RTT for an extensive property B with corresponding intensive (per-unit-mass) property $\beta = dB/dm$ is expressed as:

$$\frac{d}{dt}\int_{\Omega} \beta\rho \, d\Omega = \int_{\Omega} \frac{\partial}{\partial t}(\beta\rho) \, d\Omega + \int_{\partial\Omega} \beta\rho(\mathbf{u}\cdot\mathbf{n}) \, dS,$$

where ρ is the density, $\mathbf{u}$ is the velocity vector, and $\mathbf{n}$ is the outward unit normal on the control surface. By choosing $\beta = 1$, $\beta = \mathbf{u}$, and $\beta = e + \frac{1}{2}|\mathbf{u}|^2$, we obtain the integral forms of the conservation of mass, momentum, and energy, respectively. Applying the divergence theorem to these integral statements and assuming an arbitrary control volume yields the corresponding differential equations presented in the next section.

2.1.3 Conservation Laws

The governing equations of fluid mechanics derive from the fundamental conservation laws of physics, which represent mathematical statements of the principles of mass, momentum, and energy conservation [26].

2.1.3.1 Conservation of Mass

The continuity equation expresses the conservation of mass, stating that the rate of mass accumulation within a control volume equals the net mass flux through its boundaries.

It is stated as:

$$\frac{\partial\rho}{\partial t} + \nabla\cdot(\rho\mathbf{u}) = 0. \tag{2.2}$$

For incompressible flows, where density remains constant along fluid particle paths, this simplifies to:

$$\nabla \cdot \mathbf{u} = 0. \tag{2.3}$$

This divergence-free condition represents a kinematic constraint on the velocity field [28].

2.1.3.2 Conservation of Linear Momentum

The Cauchy momentum equation describes the balance of linear momentum, derived from Newton's second law applied to a continuum. It is stated as:

$$\rho \left(\frac{\partial \mathbf{u}}{\partial t} + (\mathbf{u} \cdot \nabla)\mathbf{u} \right) = \nabla \cdot \boldsymbol{\sigma} + \mathbf{f}_b \tag{2.4}$$

where $\boldsymbol{\sigma}$ is the Cauchy stress tensor and $\mathbf{f}_b$ represents body forces per unit volume, including gravitational, electromagnetic, and other external forces [29].

2.1.3.3 Conservation of Energy

The first law of thermodynamics yields the energy equation, expressing that the rate of change of total energy equals the work done by surface and body forces plus the heat added to the system. Given as:

$$\rho \frac{De}{Dt} = \boldsymbol{\sigma} : \nabla \mathbf{u} - \nabla \cdot \mathbf{q} + \rho r, \tag{2.5}$$

where e, is the specific internal energy, $\mathbf{q}$ is the heat flux vector, and r represents internal heat generation [30].

2.1.4 Stress and Strain Relationships

For Newtonian fluids, the constitutive relation between stress and strain rate is given by the generalized Newton's law of viscosity. This constitutive relation is

expressed as:

$$\boldsymbol{\sigma} = -p\mathbf{I} + \lambda(\nabla \cdot \mathbf{u})\mathbf{I} + 2\eta\mathbf{D}, \tag{2.6}$$

where p is the thermodynamic pressure, $\mathbf{I}$ is the identity tensor, λ is the bulk viscosity, η is the dynamic viscosity, and $\mathbf{D} = \frac{1}{2}(\nabla\mathbf{u} + (\nabla\mathbf{u})^T)$ is the strain rate tensor [31]. The decomposition of the stress tensor into isotropic and deviatoric parts reveals the fundamental response of fluids to deformation. i.e.

$$\boldsymbol{\sigma} = -p\mathbf{I} + \boldsymbol{\tau}, \tag{2.7}$$

where $\boldsymbol{\tau}$, represents the deviatoric stress tensor responsible for viscous dissipation [25].

2.2 Micropolar Fluid Theory

In this section basics of micropolar fluid theory is described.

2.2.1 Basic Concepts and Postulates

Definition: A micropolar fluid is a non-Newtonian fluid characterized by the presence of microstructures that possess independent rotational degrees of freedom. Unlike classical Newtonian fluids, which transmit only force stresses, micropolar fluids transmit both force stresses and couple stresses, resulting in a non-symmetric stress tensor. Mathematically, the fluid is described by two independent kinematic fields: the translational velocity $\mathbf{u}(\mathbf{x}, t)$ and the microrotation velocity $\mathbf{W}(\mathbf{x}, t)$, representing the intrinsic angular momentum of microelements.

The theory of micropolar fluids, introduced by Eringen, extends classical fluid mechanics by incorporating the microstructure of the fluid [8]. According to Eringen, the fundamental postulates of micropolar fluid theory include:

i. Each fluid particle possesses finite size and microstructure, behaving as a rigid body with independent rotational degrees of freedom.

ii. Particles undergo both translational and rotational motion, with the rotational motion described by an independent kinematic vector called the microrotation vector.

iii. The stress tensor is generally non-symmetric, reflecting the presence of internal moments and couple stresses.

iv. Conservation of angular momentum includes contributions from body couples and couple stresses, requiring additional balance laws.

The kinematic variables in the micropolar fluid theory are described as [8]:

i. Translational velocity: The vector $\mathbf{u}(\mathbf{x}, t)$ is representing the velocity of the particle.

ii. Microrotation velocity: The vector $\mathbf{W}(\mathbf{x}, t)$ is representing the rotational velocity of the particles.

iii. Vorticity: The vector $\boldsymbol{\omega} = \frac{1}{2}\nabla \times \mathbf{u}$ is representing the macroscopic rotation.

2.2.2 Micro-rotation and Micro-inertia

The microrotation vector $\mathbf{W}$ represents the angular velocity of the microstructured fluid particle, which is kinematically distinct from the macroscopic vorticity $\boldsymbol{\omega}$. This distinction allows micropolar fluids to model materials where the internal rotation differs from the average rotation of the fluid element.

The micro-inertia density j characterizes the resistance of micro-elements to rotational acceleration, defined as the moment of inertia per unit mass. For spherical particles of radius a, the micro-inertia is given by $j = \frac{2}{5}a^2$, while for non-spherical particles, it is described by the micro-inertia tensor i_{kl}. [8].

The micro-inertia tensor satisfies the conservation equation:

$$\frac{Di_{kl}}{Dt} + i_{km}\epsilon_{mlr}W_r + i_{lm}\epsilon_{mkr}W_r = 0 \tag{2.8}$$

This equation governs how the micro-inertia tensor evolves along a particle path due to the microrotation field. The terms involving the Levi-Civita symbol account for the rotational transformation of the inertia tensor as the microelements rotate in space. In the above equation, ϵ_{mlr} and ϵ_{mkr} denote the Levi-Civita permutation symbol, a fully antisymmetric tensor defined as:

$$\epsilon_{ijk} = \begin{cases} +1, & \text{if } (i,j,k) \text{ is an even permutation of } (1,2,3), \\ -1, & \text{if } (i,j,k) \text{ is an odd permutation of } (1,2,3), \\ 0, & \text{if any two indices are equal.} \end{cases}$$

The permutation symbol introduces antisymmetric coupling terms such as

$i_{km}\epsilon_{mlr}W_r$, which represent cross-product-type interactions between the micro-inertia tensor and the microrotation field.

2.3 Eringen's Theory and Governing Equations

Eringen's theory [8] of micropolar fluids introduces additional balance laws and constitutive equations that extend the classical Navier-Stokes framework . The complete set of governing equations are stated as follows.

2.3.1 Conservation of Mass

The conservation of mass is stated as

$$\frac{\partial \rho}{\partial t} + \nabla \cdot (\rho \mathbf{u}) = 0. \tag{2.9}$$

This equation remains identical to equation 2.2 in classical continuum mechanics.

2.3.2 Conservation of Linear Momentum

The equation of conservation of linear momentum is stated as

$$\rho \frac{D\mathbf{u}}{Dt} = \nabla \cdot \boldsymbol{\sigma} + \rho \mathbf{f}, \tag{2.10}$$

where, the stress tensor $\boldsymbol{\sigma}$ is generally non-symmetric, reflecting the presence of internal moments.

2.3.3 Conservation of Angular Momentum

The equation of conservation of angular momentum is stated as

$$\rho j \frac{D\mathbf{W}}{Dt} = \nabla \cdot \mathbf{m} + \boldsymbol{\sigma}_{\times} + \rho \mathbf{l}, \tag{2.11}$$

where $\mathbf{m}$ is the couple stress tensor, $\boldsymbol{\sigma}_{\times}$ is the vector invariant of the stress tensor ($\boldsymbol{\sigma}_{\times} = \epsilon : \boldsymbol{\sigma}$), and $\mathbf{l}$ is the body couple per unit mass.

2.4 Constitutive Relations for Stress and Couple Stress

For linear isotropic micropolar fluids, the constitutive equations are derived from thermodynamic principles and material frame indifference. These constitutive relations are stated given as:

$$\boldsymbol{\sigma} = (-p + \lambda \nabla \cdot \mathbf{u})\mathbf{I} + 2\eta \mathbf{D} + 2\eta_r(\mathbf{A} - \boldsymbol{\Omega}), \tag{2.12}$$

$$\mathbf{m} = \alpha(\nabla \cdot \mathbf{W})\mathbf{I} + \beta \nabla \mathbf{W} + \gamma(\nabla \mathbf{W})^T, \tag{2.13}$$

where, η is the Newtonian dynamic viscosity, representing the resistance to shear deformation, η_r is the microrotational viscosity, characterizing resistance to relative rotation between micro-elements, $\mathbf{A}$ is the antisymmetric part of the velocity gradient tensor, $\mathbf{\Omega}$ is the angular velocity tensor associated with microrotation, α, β, γ are the coefficients of angular viscosities, satisfying thermodynamic constraints [8].

The Clausius-Duhem inequality imposes restrictions on the viscosity coefficients. i.e.

$$\eta \geq 0, \quad \eta_r \geq 0, \quad 3\lambda + 2\eta \geq 0, \tag{2.14}$$

$$\gamma \geq 0, \quad 3\alpha + \beta + \gamma \geq 0, \quad \beta + \gamma \geq 0. \tag{2.15}$$

2.5 Physical Interpretation of Micropolar Parameters

The micropolar theory introduces several important dimensionless parameters that characterize the microstructural effects [2, 3]. Recent studies have applied these concepts to turbulent flows [32] and magnetohydrodynamic (MHD) problems with variable thermal conductivity [33].

2.5.1 Micropolar Parameter

The micropolar parameter K is defined as:

$$K = \frac{\eta_r}{\eta}, \tag{2.16}$$

where, η_r is microrotational viscosity and η is Newtonian viscosity. This parameter represents the ratio of microrotational viscosity to Newtonian viscosity, characterizing the strength of micropolar effects relative to classical viscous effects [34].

If $K = 0$, the fluid is Newtonian (no micropolar effects).

If $0 < K < 1$, the fluid has Weak micropolar effects.

If $K \approx 1$, the viscous and micropolar effects are comparable.

If $K > 1$, the fluid has dominant microrotational effects.

2.5.2 Spin Gradient Viscosity Parameter

The spin gradient viscosity parameter is defined as [33]:

$$K_m = \frac{\gamma}{\eta j} \approx 1 + \frac{K}{2}. \tag{2.17}$$

This parameter relates the spin gradient viscosity γ to the Newtonian viscosity η and micro-inertia j, influencing the diffusion of microrotation [34].

2.5.3 Eringen Number

The Eringen number defined as [34]:

$$Er = \frac{j}{L^2}, \tag{2.18}$$

where L is the characteristic length scale and j is micro-inertia. This parameter represents the relative importance of micro-inertia effects compared to the system size [32].

2.6 Magnetohydrodynamics

In this section the theory of megnetohydrodynamics is described.

2.6.1 Maxwell's Equations for Electromagnetic Fields

The behavior of electromagnetic fields in continuous media is governed by Maxwell's equations, which form the foundation of classical electrodynamics [35].

2.6.1.1 Gauss's Law for Electricity

$$\nabla \cdot \mathbf{E} = \frac{\rho_e}{\epsilon_0}, \tag{2.19}$$

where, $\mathbf{E}$ is the electric field intensity, ρ_e is the electric charge density, and ϵ_0 is the permittivity of free space [36].

2.6.1.2 Gauss's Law for Magnetism

The Gauss's law of magnetism is stated as:

$$\nabla \cdot \mathbf{B} = 0, \tag{2.20}$$

where, $\mathbf{B}$ is the magnetic flux density, indicating the absence of magnetic monopoles.

2.6.1.3 Faraday's Law of Induction

The Faraday's law of induction is stated as

$$\nabla \times \mathbf{E} = -\frac{\partial \mathbf{B}}{\partial t}. \tag{2.21}$$

This equation describes how a time-varying magnetic field induces an electric field [36].

2.6.1.4 Ampère-Maxwell Law

The Ampère-Maxwell law stated as

$$\nabla \times \mathbf{B} = \mu_0 \left(\mathbf{J} + \epsilon_0 \frac{\partial \mathbf{E}}{\partial t} \right), \tag{2.22}$$

where, $\mathbf{J}$ is the current density and μ_0 is the permeability of free space [35].

2.6.2 Ohm's Law for Moving Media

For a moving conducting fluid, Ohm's law generalizes to account for the motion-induced electromotive force.

$$\mathbf{J} = \sigma(\mathbf{E} + \mathbf{u} \times \mathbf{B}) \tag{2.23}$$

where, σ is the electrical conductivity of the fluid. This formulation assumes isotropic electrical properties and neglects Hall effects and ion slip [4].

2.6.3 Lorentz Force and Its Effects

The Lorentz force per unit volume acting on the fluid represents the electromagnetic body force.

$$\mathbf{F}_L = \mathbf{J} \times \mathbf{B}. \tag{2.24}$$

Substituting Ohm's law yields the following general expression.

$$\mathbf{F}_L = \sigma(\mathbf{E} + \mathbf{u} \times \mathbf{B}) \times \mathbf{B}. \tag{2.25}$$

For cases where the electric field is negligible or aligned with the magnetic field, this simplifies to.

$$\mathbf{F}_L = \sigma(\mathbf{u} \times \mathbf{B}) \times \mathbf{B}. \tag{2.26}$$

The Lorentz force can be decomposed into components parallel and perpendicular to the magnetic field, leading to both resistive and inductive effects on the flow [4].

2.6.4 Magnetic Induction Equations

The induction equation describes the evolution of the magnetic field in a moving conducting fluid, derived from Maxwell's equations and Ohm's law

$$\frac{\partial \mathbf{B}}{\partial t} = \nabla \times (\mathbf{u} \times \mathbf{B}) + \frac{1}{\mu_0 \sigma} \nabla^2 \mathbf{B}. \tag{2.27}$$

This equation represents the competition between advection (first term) and diffusion (second term) of the magnetic field [37].

2.7 Thermal Radiation

This section describes the concept of thermal radiation.

2.7.1 Fundamentals of Radiative Heat Transfer

Thermal radiation is the energy transfer by electromagnetic waves due to temperature differences, governed by the laws of thermodynamics and electromagnetism. Unlike conduction and convection, radiation does not require a medium and can occur in vacuum, making it particularly important in high-temperature applications [38].

2.7.2 Rosseland Approximation for Optically Thick Media

For optically thick media where the mean free path of photons is small compared to the characteristic length scale, the Rosseland diffusion approximation is applicable.

This approximation assumes that radiation is a diffusion process similar to heat conduction, valid when the optical thickness $\tau = \beta L \gg 1$. The radiative heat flux is given by

$$\mathbf{q}_r = -\frac{16\sigma^* T^3}{3\beta_R}\nabla T, \tag{2.28}$$

where, $\sigma^* = 5.67 \times 10^{-8}\mathrm{W/m^2K^4}$ is the Stefan-Boltzmann constant and β_R is the Rosseland mean absorption coefficient.

The divergence of the radiative heat flux becomes

$$\nabla \cdot \mathbf{q}_r = -\nabla \cdot (\kappa_r \nabla T)\,, \tag{2.29}$$

where, $\kappa_r = \frac{16\sigma^* T^3}{3\beta_R}$ is the radiative conductivity, which depends strongly on temperature [38].

2.7.3 Radiative Heat Flux Modeling

For participating media, the total heat flux comprises conductive and radiative components as

$$\mathbf{q} = \mathbf{q}_c + \mathbf{q}_r = -\kappa\nabla T - \frac{16\sigma^* T^3}{3\beta_R}\nabla T. \tag{2.30}$$

This formulation shows that radiation contributes to heat transfer in a manner similar to conduction, but with a strongly temperature-dependent coefficient. The radiative conductivity increases with the cube of temperature, making it particularly significant in high-temperature applications.

This leads to an effective thermal conductivity that combines molecular and radiative transport given as

$$\kappa_{eff} = \kappa + \kappa_r = \kappa + \frac{16\sigma^* T^3}{3\beta_R}. \tag{2.31}$$

The temperature dependence of radiative conductivity makes the energy equation nonlinear, requiring iterative solution methods [38].

2.7.4 Combined Radiation and Convection

In energy transport involving both radiation and convection, the energy equation becomes

$$\rho c_p \frac{DT}{Dt} = \nabla \cdot (\kappa \nabla T) - \nabla \cdot \mathbf{q}_r + \Phi + Q, \tag{2.32}$$

where, Φ is the viscous dissipation function and Q represents other heat sources [30]. The relative importance of radiation to conduction is characterized by the conduction-radiation parameter

$$N_{CR} = \frac{\kappa \beta_R}{4\sigma^* T^3}. \tag{2.33}$$

Small values of N_{CR} indicate radiation-dominated heat transfer, while large values indicate conduction-dominated transport [38].

2.8 The Finite Element Method

The finite element method is a powerful numerical technique for solving partial differential equations, particularly well-suited for problems involving complex geometries, heterogeneous materials, and multiphysics couplings. The method approximates the solution by dividing the computational domain into smaller subdomains called *elements*, over which piecewise polynomial approximations are used [22].

The procedure is demonstrated through the following example problem.

2.8.1 Problem: Steady Heat Conduction

To illustrate the finite element method in a simple setting, consider the one-dimensional steady heat conduction problem on the unit interval $\Omega = (0, 1)$:

$$-\frac{d}{dx}\left(k\frac{du}{dx}\right) = f(x), \quad x \in (0, 1),$$

with constant thermal conductivity $k = 1$ and source term $f(x) = 2$. The boundary conditions are Dirichlet:

$$u(0) = 0, \quad u(1) = 1.$$

The exact solution can be obtained by integrating twice:

$$u_{\text{exact}}(x) = -x^2 + 2x.$$

i) Weak Formulation.

Multiply the differential equation by a test function $v(x)$ that vanishes on the Dirichlet boundaries ($v(0) = v(1) = 0$), integrate over the domain, and apply integration by parts:

$$\int_0^1 -\frac{d^2u}{dx^2}\, v\, dx = \int_0^1 2v\, dx.$$

Integration by parts gives:

$$\left[-\frac{du}{dx}v\right]_0^1 + \int_0^1 \frac{du}{dx}\frac{dv}{dx}\, dx = \int_0^1 2v\, dx.$$

The boundary term vanishes because $v(0) = v(1) = 0$. Thus the weak form is: find $u \in H_0^1(0,1)$ such that:

$$\int_0^1 \frac{du}{dx}\frac{dv}{dx}\, dx = \int_0^1 2v\, dx \quad \forall v \in H_0^1(0,1).$$

ii) Finite Element Discretization.

Partition the interval $[0,1]$ into N elements of equal length $h = 1/N$. Let the nodes be $x_i = ih$ for $i = 0, 1, \ldots, N$. We seek an approximate solution u_h that is continuous and piecewise linear on each element. On each element $[x_i, x_{i+1}]$, we write

$$u_h(x) = U_i\phi_i(x) + U_{i+1}\phi_{i+1}(x),$$

where ϕ_i are the linear shape functions satisfying $\phi_i(x_j) = \delta_{ij}$. Specifically, on element e spanning $[x_i, x_{i+1}]$,

$$\phi_i(x) = \frac{x_{i+1} - x}{h}, \quad \phi_{i+1}(x) = \frac{x - x_i}{h}.$$

The test functions v_h are taken from the same space, i.e.,
$v_h(x) = \sum_{i=1}^{N-1} V_i \phi_i(x)$ (note that $V_0 = V_N = 0$ due to Dirichlet conditions).

Substituting into the weak form and choosing each basis function as test function yields a linear system. For a typical interior node j $(1 \leq j \leq N-1)$, the equation is:

$$\sum_{i=1}^{N-1} U_i \int_0^1 \frac{d\phi_i}{dx} \frac{d\phi_j}{dx}\, dx = \int_0^1 2\phi_j\, dx.$$

We assemble the global stiffness matrix and load vector by summing contributions from each element.

iii) Element Matrices.

On a typical element e with nodes i and $i+1$, the local stiffness matrix entries are:

$$K_{ii}^{(e)} = \int_{x_i}^{x_{i+1}} \left(\frac{d\phi_i}{dx}\right)^2 dx = \int_{x_i}^{x_{i+1}} \left(-\frac{1}{h}\right)^2 dx = \frac{1}{h},$$

$$K_{i,i+1}^{(e)} = \int_{x_i}^{x_{i+1}} \frac{d\phi_i}{dx}\frac{d\phi_{i+1}}{dx} dx = \int_{x_i}^{x_{i+1}} \left(-\frac{1}{h}\right)\left(\frac{1}{h}\right) dx = -\frac{1}{h},$$

$$K_{i+1,i}^{(e)} = K_{i,i+1}^{(e)} = -\frac{1}{h}, \quad K_{i+1,i+1}^{(e)} = \frac{1}{h}.$$

The local load vector components are:

$$F_i^{(e)} = \int_{x_i}^{x_{i+1}} 2\phi_i\, dx = 2\int_{x_i}^{x_{i+1}} \frac{x_{i+1} - x}{h}\, dx = 2 \cdot \frac{h}{2} = h,$$

$$F_{i+1}^{(e)} = \int_{x_i}^{x_{i+1}} 2\phi_{i+1}\, dx = 2 \cdot \frac{h}{2} = h.$$

iv) Assembly and Solution.

Assembling for all elements gives the global system $\mathbf{KU} = \mathbf{F}$. For example, with $N = 4$ elements ($h = 0.25$), the system for interior nodes U_1, U_2, U_3 (with $U_0 = 0$, $U_4 = 1$ known) becomes:

$$\begin{bmatrix} \frac{2}{h} & -\frac{1}{h} & 0 \\ -\frac{1}{h} & \frac{2}{h} & -\frac{1}{h} \\ 0 & -\frac{1}{h} & \frac{2}{h} \end{bmatrix} \begin{bmatrix} U_1 \\ U_2 \\ U_3 \end{bmatrix} = \begin{bmatrix} h \\ h \\ h \end{bmatrix} - \begin{bmatrix} -\frac{1}{h}U_0 \\ 0 \\ -\frac{1}{h}U_4 \end{bmatrix}.$$

The right-hand side includes the known boundary values. Solving yields the nodal temperatures. Table 2.1 compares the finite element solution at the nodes with the exact solution for $h = 0.25$.

x	U_h	u_{exact}	Error
0.00	0.0000	0.0000	0.0000
0.25	0.4375	0.4375	0.0000
0.50	0.7500	0.7500	0.0000
0.75	0.9375	0.9375	0.0000
1.00	1.0000	1.0000	0.0000

TABLE 2.1: Comparison of FEM solution with exact solution for 1D heat conduction with $f(x) = 2$. The FEM exactly reproduces the quadratic solution because the exact solution is quadratic and linear elements on a uniform mesh can represent it exactly (the error is zero at nodes).

For a more general source term, the FEM would give approximate values, and convergence can be studied. This simple example demonstrates the key steps: weak formulation, discretization, element matrices, assembly, and solution.

Chapter 3

Reproduction of Turek and Schäfer Benchmark Case 2D-2

3.1 Introduction

The validation of numerical methodologies against established benchmark problems is essential for ensuring the reliability and accuracy of computational simulations. Among the most widely recognized benchmarks in computational fluid dynamics is the work of Turek and Schäfer [21], which emerged from the Deutsche Forschungsgemeinschaft (DFG) priority research program "Flow Simulation with High-Performance Computers" conducted between 1993 and 1995. This collaborative program brought together numerous research groups to develop and evaluate numerical methods for incompressible flow problems, with the goal of establishing reference solutions that could serve as standard test cases for code validation.

The benchmark paper by Turek and Schäfer, along with their colleagues, presented a series of carefully defined test problems for laminar flow configurations. Among these, the two-dimensional flow around a circular cylinder in a channel designated as Benchmark 2D-2 has become particularly influential.

The problem was deliberately designed to capture essential flow features including boundary layer development, flow separation, vortex shedding, and fluid-structure interaction, while maintaining geometric simplicity. The cylinder is placed asymmetrically in the channel to break symmetry and trigger unsteady behavior at moderate Reynolds numbers.

What makes this benchmark particularly valuable is the comprehensive set of reference data provided by the authors. Drawing upon contributions from multiple research groups using different numerical approaches (finite volumes, finite elements, and spectral methods), the paper reports quantitative results including drag and lift coefficients, pressure differences, and Strouhal numbers for Reynolds numbers ranging from 20 to 200. For the unsteady case at $Re = 100$, which is the focus of this chapter, the benchmark provides time histories of force coefficients and pressure values that have become standard reference data for code validation worldwide.

The benchmark's enduring influence stems from several factors. First, the problem captures complex but well-understood physics the periodic von Kármán vortex street that develops behind the cylinder. Second, the geometry is simple enough to mesh easily but includes features like curved boundaries that test a method's geometric flexibility. Third, the reference data includes both integral quantities (forces) and local values (pressures at specific points), allowing comprehensive validation. Finally, the collaborative nature of the original study, with results from multiple independent codes, provides confidence in the reference values.

This chapter presents the reproduction and validation of this well established benchmark case using the numerical methodology employed in this research. The primary objectives are threefold: to implement and validate the numerical methodology against an established standard, to establish confidence in the computational framework for subsequent complex simulations, and to provide reference solutions for comparison with future studies involving micropolar and magnetohydrodynamic effects. The successful reproduction of this benchmark case at Reynolds number $Re = 100$ demonstrates the reliability of the computational framework

and provides a solid foundation for the more complex multiphysics simulations presented in Chapter 4.

3.2 Benchmark Problem Description

This section describes the geometry, boundary conditions, and fluid properties of the benchmark problem. The configuration follows the specifications of the Turek and Schäfer benchmark case 2D-2, ensuring consistency with established reference data. This benchmark problem is widely used in computational fluid dynamics to validate numerical methods for laminar flow around bluff bodies. It provides a rigorous test for code accuracy by comparing key quantities such as drag and lift coefficients, pressure differences, and vortex shedding frequencies.

3.2.1 Geometry and Flow Configuration

The Benchmark 2D-2 concerns two-dimensional laminar flow around a circular cylinder placed in a channel. The geometry and dimensions follow the specifications established by Turek and Schäfer and are illustrated in Figure 3.1.

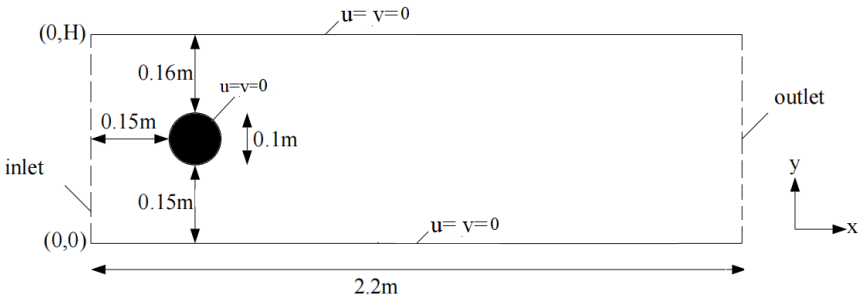

FIGURE 3.1: Geometry and dimensions for the Turek and Schäfer benchmark case 2D-2. The cylinder of diameter $D = 0.1$ m is positioned asymmetrically in a channel of height $H = 0.41$ m.

The geometrical parameters are listed as follows

i) Channel height: $H = 0.41$ m.

ii) Channel length: $L = 2.2$ m (from inlet to outlet).

iii) Cylinder diameter: $D = 0.1$ m.

iv) Cylinder center position: $(0.2, 0.2)$ m from bottom left corner.

v) Domain dimensions: 2.2×0.41 m.

The asymmetric placement of the cylinder induces complex flow phenomena including flow separation, and vortex shedding, making this an excellent test case for validating numerical methods [21].

3.2.2 Boundary Conditions

The boundary conditions implemented for this benchmark problem follow the original specifications. At the inlet, a fully developed parabolic velocity profile is prescribed, corresponding to laminar channel flow. On the channel walls and cylinder surface, no-slip conditions are imposed, while at the outlet a stress-free boundary condition is applied to allow smooth outflow without influencing the upstream flow [21].

Inlet Boundary Condition:
A parabolic velocity profile is prescribed at the inlet:

$$U(0, y) = \frac{4U_m y(H - y)}{H^2}, \quad V(0, y) = 0, \tag{3.1}$$

where, $U_m = 1.5$ m/s is the maximum inflow velocity. The mean inflow velocity is defined as:

$$\bar{U} = \frac{2}{3}U(0, H/2) \approx 1.0 \text{ m/s}. \tag{3.2}$$

Outlet Boundary Condition:
The following "do-nothing" outflow condition is applied at the outlet:

$$\eta \frac{\partial \mathbf{u}}{\partial \mathbf{n}} - p\mathbf{n} = 0. \tag{3.3}$$

This condition allows for smooth outflow while maintaining global mass conservation.

Wall Boundary conditions:

No-slip conditions are applied on the upper and lower channel walls. i.e.

$$\mathbf{u} = 0, \quad \text{on} \quad \Gamma_{\text{wall}} \tag{3.4}$$

Cylinder Surface:

No-slip condition is applied on the cylinder surface. i.e.

$$\mathbf{u} = 0. \quad \text{on} \quad \Gamma_{\text{cylinder}} \tag{3.5}$$

3.2.3 Fluid Properties and Flow Parameters

The fluid properties are chosen to match the benchmark specifications for case 2D-2. The density of the fluid is taken $\rho = 1.0$ kg/m^3, the dynamic viscosity is $\eta = 0.001$ Pa·s and the kinematic viscosity is $\nu = 0.001$ m^2/s. The Reynold number based on cylinder diameter and mean velocity is given as

$$Re = \frac{\rho \bar{U} D}{\eta} = \frac{1.0 \times 1.0 \times 0.1}{0.001} = 100. \tag{3.6}$$

This Reynold number ensures unsteady laminar flow with periodic vortex shedding, providing a challenging test case for numerical methods.

3.3 Mathematical Formulation of the Benchmark Problem

This section presents the complete mathematical framework governing the fluid flow simulations, including the governing equations, non-dimensionalization procedure, weak formulation, and force calculations. The formulation follows established practices for incompressible Navier-Stokes equations and is tailored for finite

element implementation.

3.3.1 Governing Equations

The flow of an incompressible Newtonian fluid is governed by the Navier-Stokes equations, which express conservation of mass and momentum.

3.3.1.1 The Vector Form of Governing Equations

The conservation equations in vector form are described as following:

The conservation of mass is given as:

$$\nabla \cdot \mathbf{U} = 0. \tag{3.7}$$

The conservation of momentum is stated as:

$$\rho \left(\frac{\partial \mathbf{U}}{\partial t} + (\mathbf{U} \cdot \nabla)\mathbf{U} \right) = -\nabla P + \eta \nabla^2 \mathbf{U}, \tag{3.8}$$

where, $\mathbf{U} = (U, V)$ is the dimensional velocity vector, P is the pressure, ρ is the density, η is the dynamic viscosity, and t is time.

3.3.1.2 The Component Form of Governing Equations

In Cartesian coordinates, the component form of governing equations are stated as follows.

The continuity equation, which expresses conservation of mass, is given by:

$$\frac{\partial U}{\partial X} + \frac{\partial V}{\partial Y} = 0. \tag{3.9}$$

The X-momentum equation, representing conservation of linear momentum in the horizontal direction, reads:

$$\rho\left(\frac{\partial U}{\partial \tilde{T}}+U\frac{\partial U}{\partial X}+V\frac{\partial U}{\partial Y}\right)=-\frac{\partial P}{\partial X}+\eta\left(\frac{\partial^2 U}{\partial X^2}+\frac{\partial^2 U}{\partial Y^2}\right). \tag{3.10}$$

Similarly, the Y-momentum equation for the vertical direction is expressed as:

$$\rho\left(\frac{\partial V}{\partial \tilde{T}}+U\frac{\partial V}{\partial X}+V\frac{\partial V}{\partial Y}\right)=-\frac{\partial P}{\partial Y}+\eta\left(\frac{\partial^2 V}{\partial X^2}+\frac{\partial^2 V}{\partial Y^2}\right). \tag{3.11}$$

3.3.2 Non-Dimensionalization

Following the benchmark problem of Turek and Schäfer [21], the equations are non-dimensionalized using characteristic scales relevant to flow past a circular cylinder.The reference quantities are chosen based on the following benchmark specifications:

i) Characteristic length: $D = 0.1$ m (cylinder diameter).

ii) Characteristic velocity: $\bar{U} = 1.0$ m/s (mean inflow velocity).

iii) Characteristic time: $D/\bar{U}$.

iv) Characteristic pressure: $\rho\bar{U}^2$.

The dimensionless variables are defined as:

$$x=\frac{X}{D},\qquad y=\frac{Y}{D},\qquad t=\frac{\tilde{T}\bar{U}}{D},\qquad u=\frac{U}{\bar{U}},\qquad v=\frac{V}{\bar{U}},\qquad p=\frac{P}{\rho\bar{U}^2} \tag{3.12}$$

The Reynolds number, representing the ratio of inertial to viscous forces, is defined as

$$Re=\frac{\rho\bar{U}D}{\eta}=\frac{\bar{U}D}{\nu}, \tag{3.13}$$

where, $\nu = \eta/\rho$ is the kinematic viscosity.

3.3.2.1 The Dimensionless Equations of Benchmark Problem

Substituting the dimensionless variables defined in equation (3.12) into the governing equations (3.9)–(3.11) yields the following non-dimensional form.
The dimensionless continuity reads:

$$\frac{\partial u}{\partial x} + \frac{\partial v}{\partial y} = 0. \tag{3.14}$$

The dimensionless X-momentum reads:

$$\frac{\partial u}{\partial t} + u\frac{\partial u}{\partial x} + v\frac{\partial u}{\partial y} = -\frac{\partial p}{\partial x} + \frac{1}{Re}\left(\frac{\partial^2 u}{\partial x^2} + \frac{\partial^2 u}{\partial y^2}\right). \tag{3.15}$$

The dimensionless Y-momentum reads:

$$\frac{\partial v}{\partial t} + u\frac{\partial v}{\partial x} + v\frac{\partial v}{\partial y} = -\frac{\partial p}{\partial y} + \frac{1}{Re}\left(\frac{\partial^2 v}{\partial x^2} + \frac{\partial^2 v}{\partial y^2}\right). \tag{3.16}$$

3.3.3 Weak Formulation

The finite element method requires the weak (variational) form of the governing equations. Let $(\tilde{u}, \tilde{v}, \tilde{p})$ be test functions for the velocity components and pressure, respectively, belonging to appropriate function spaces.
The time discretization is achieved by using the backward Euler method as:

$$\frac{\partial u}{\partial t} \approx \frac{u^{n+1} - u^n}{\delta t}, \quad \frac{\partial v}{\partial t} \approx \frac{v^{n+1} - v^n}{\delta t} \tag{3.17}$$

where, δt is the time step, and superscripts denote time levels.
Now, multiplying the dimensionless continuity equation (3.14) at time level t^{n+1} by the test function $\tilde{p}$ and integrating over the domain Ω^{n+1}, we obtain:

$$\int_{\Omega^{n+1}} \left(\frac{\partial u^{n+1}}{\partial x^{n+1}} + \frac{\partial v^{n+1}}{\partial y^{n+1}}\right) \tilde{p}\, d\Omega = 0. \tag{3.18}$$

Also, multiplying the dimensionless X-momentum equation (3.15) at time level t^{n+1} by the test function $\tilde{u}$ and integrating over the domain Ω^{n+1}, we obtain:

$$\int_{\Omega^{n+1}} \frac{u^{n+1}-u^n}{\delta t}\,\tilde{u}\,d\Omega + \int_{\Omega^{n+1}} \left(u^n \frac{\partial u^{n+1}}{\partial x^{n+1}} + v^n \frac{\partial u^{n+1}}{\partial y^{n+1}}\right)\tilde{u}\,d\Omega$$
$$= -\int_{\Omega^{n+1}} \frac{\partial p^{n+1}}{\partial x^{n+1}}\tilde{u}\,d\Omega + \frac{1}{Re}\int_{\Omega^{n+1}} \nabla^2 u^{n+1}\,\tilde{u}\,d\Omega. \tag{3.19}$$

Applying integration by parts to the pressure and diffusion terms:

$$\frac{1}{\delta t}\int_{\Omega^{n+1}} u^{n+1}\tilde{u}\,d\Omega + \int_{\Omega^{n+1}} \left(u^n \frac{\partial u^{n+1}}{\partial x^{n+1}} + v^n \frac{\partial u^{n+1}}{\partial y^{n+1}}\right)\tilde{u}\,d\Omega$$
$$+ \int_{\Omega^{n+1}} p^{n+1}\frac{\partial \tilde{u}}{\partial x^{n+1}}\,d\Omega + \frac{1}{Re}\int_{\Omega^{n+1}} \left(\frac{\partial u^{n+1}}{\partial x^{n+1}}\frac{\partial \tilde{u}}{\partial x^{n+1}} + \frac{\partial u^{n+1}}{\partial y^{n+1}}\frac{\partial \tilde{u}}{\partial y^{n+1}}\right)d\Omega$$
$$= \frac{1}{\delta t}\int_{\Omega^{n+1}} u^n\tilde{u}\,d\Omega + \int_{\Gamma^{n+1}} p^{n+1}\tilde{u}n_x\,d\Gamma - \frac{1}{Re}\int_{\Gamma^{n+1}} \frac{\partial u^{n+1}}{\partial n}\tilde{u}\,d\Gamma. \tag{3.20}$$

Similarly, for the Y-momentum equation we can write:

$$\frac{1}{\delta t}\int_{\Omega^{n+1}} v^{n+1}\tilde{v}\,d\Omega + \int_{\Omega^{n+1}} \left(u^n \frac{\partial v^{n+1}}{\partial x^{n+1}} + v^n \frac{\partial v^{n+1}}{\partial y^{n+1}}\right)\tilde{v}\,d\Omega$$
$$+ \int_{\Omega^{n+1}} p^{n+1}\frac{\partial \tilde{v}}{\partial y^{n+1}}\,d\Omega + \frac{1}{Re}\int_{\Omega^{n+1}} \left(\frac{\partial v^{n+1}}{\partial x^{n+1}}\frac{\partial \tilde{v}}{\partial x^{n+1}} + \frac{\partial v^{n+1}}{\partial y^{n+1}}\frac{\partial \tilde{v}}{\partial y^{n+1}}\right)d\Omega$$
$$= \frac{1}{\delta t}\int_{\Omega^{n+1}} v^n\tilde{v}\,d\Omega + \int_{\Gamma^{n+1}} p^{n+1}\tilde{v}n_y\,d\Gamma - \frac{1}{Re}\int_{\Gamma^{n+1}} \frac{\partial v^{n+1}}{\partial n}\tilde{v}\,d\Gamma. \tag{3.21}$$

3.3.4 Drag and Lift Forces

The hydrodynamic forces on the cylinder are crucial quantities of interest that serve as primary validation metrics for this benchmark study. The drag and lift forces acting on the cylinder surface S are given by

$$F_D = \int_S \left(\rho\nu\frac{\partial v_t}{\partial n}n_y - Pn_x\right)dS, \tag{3.22}$$

and

$$F_L = -\int_S \left(\rho\nu \frac{\partial v_t}{\partial n} n_x + P n_y\right) dS, \tag{3.23}$$

where

i) $\mathbf{n} = (n_x, n_y)$ is the outward unit normal vector on S,

ii) $\mathbf{t} = (n_y, -n_x)$ is the tangential vector,

iii) v_t is the tangential velocity componentm,

iv) $\frac{\partial v_t}{\partial n}$ is the normal derivative of tangential velocity.

These formulations follow the established conventions of the Turek and Schäfer benchmark problem [21] and are particularly suitable for implementation in FreeFEM++.

3.4 Validation Metrics

The simulation results are validated against the benchmark using the following quantitative metrics

3.4.1 Drag and Lift Coefficients

The drag and lift coefficients are computed as:

$$C_D = \frac{F_D}{\frac{1}{2}\rho \bar{U}^2 D}, \tag{3.24}$$

and

$$C_L = \frac{F_L}{\frac{1}{2}\rho \bar{U}^2 D}, \tag{3.25}$$

where, F_D and F_L are the drag and lift forces on the cylinder, computed by integrating the pressure and viscous stresses over the cylinder surface.

3.4.2 Pressure Difference

The pressure difference between the front and back of the cylinder is evaluated as

$$\Delta p = p(0.15, 0.2) - p(0.25, 0.2). \tag{3.26}$$

3.5 Results and Discussion

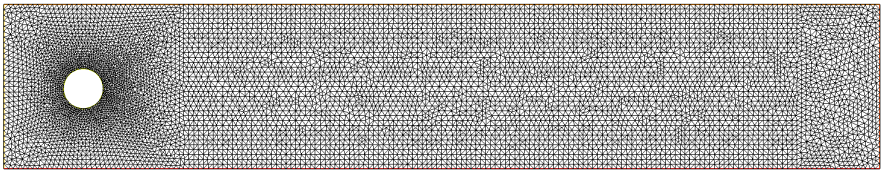

FIGURE 3.2: Triangulated computational domain with number of elements $N_{\text{el}} = 6826$.

To validate the accurate implementation the results are obtained for the cylinder-in-channel benchmark at Reynold number $Re = 100$. The computational domain and the unstructured triangular mesh used in the simulations are shown in Figure 3.2; the mesh contains 6826 elements with local refinement in the vicinity of the cylinder to resolve the boundary layer and near-wake region. All hydrodynamic quantities reported below (drag coefficient c_D, lift coefficient c_L, and the pressure difference Δp between the benchmark probe locations) are non-dimensional and computed from the surface pressure and viscous stress integrals on the cylinder boundary using the same definitions as the reference benchmark [21]. Time-dependent results are sampled at the instants shown in the tables and figures; note that instantaneous maxima are sensitive to the phase of vortex shedding, whereas cycle-averaged values are less sensitive to phase offsets.

TABLE 3.1: Maximum drag coefficient c_D at $Re = 100$.

Time (s)	Reference c_D [21]	Present c_D	Difference
10	3.2152	3.65705	0.44185
16	3.2900	3.65757	0.36757
19	3.2356	3.65757	0.42197

TABLE 3.2: Maximum lift coefficient c_L at $Re = 100$.

Time (s)	Reference c_L [21]	Present c_L	Difference
10	0.9028	1.08826	0.18546
16	1.2500	1.08829	-0.16171
19	1.0000	1.08829	0.08829

TABLE 3.3: Pressure difference Δp at $Re = 100$.

Time (s)	Reference Δp [21]	Present Δp	Difference
10	2.4715	2.34124	-0.13026
16	2.5700	2.41683	-0.15317
19	2.4871	2.34024	-0.14686

3.5.1 Quantitative Validation

Tables 3.1–3.3 present the computed values of drag coefficient (c_D), lift coefficient (c_L), and pressure difference (Δp) at different time instants for $Re = 100$. The results are compared with the benchmark data reported by Turek and Schäfer [21]. Overall, the present simulations exhibit a very good agreement with the reference data, capturing both the trend and the magnitude of the flow quantities. Minor deviations may occur due to mesh resolution near the cylinder, numerical integration accuracy, and phase differences during vortex shedding; however, the overall pattern and physical behaviour remain consistent with the benchmark.

i) Drag coefficient c_D.

The temporal variation of c_D follows the same trend as reported in the benchmark. The drag coefficient initially increases as the boundary layer develops and then exhibits small oscillations corresponding to vortex shedding in the wake.

ii) Lift coefficient c_L.

The lift coefficient demonstrates periodic fluctuations after the initial transient phase, which are characteristic of alternating vortex shedding. The amplitude and frequency of the oscillations match well with the reference data.

iii) Pressure difference Δp.

The computed pressure difference between the benchmark probe locations shows close correspondence with the reference values, indicating that the present simulation accurately resolves the pressure distribution around the cylinder.

The close resemblance between the present and reference data verifies that the numerical model, boundary conditions, and discretization techniques adopted in this study are reliable and accurate for simulating laminar flow past a confined cylinder at $Re = 100$. The agreement in drag coefficient, lift amplitude, and vortex shedding frequency demonstrates that the numerical framework accurately resolves the essential flow physics. With this established confidence, the study now proceeds to investigate the coupled effects of micropolar rheology, magnetic fields, and thermal radiation in the dual-cylinder configuration.

3.5.2 Drag and Lift Time-History Analysis

The time histories of drag and lift coefficients are shown in Figures 3.3 and 3.4. After a short transient period, both coefficients attain a nearly periodic state that corresponds to the periodic shedding of vortices in the wake. The lift coefficient oscillates symmetrically about zero, confirming the alternating nature of vortex shedding from the upper and lower cylinder surfaces. The drag coefficient, meanwhile, oscillates at twice the frequency of the lift coefficient, a well-known feature of vortex-induced forces on bluff bodies.

From Figure 3.3, the drag coefficient exhibits mild periodic oscillations superimposed on a steady mean value, which reflects the alternating vortex formation

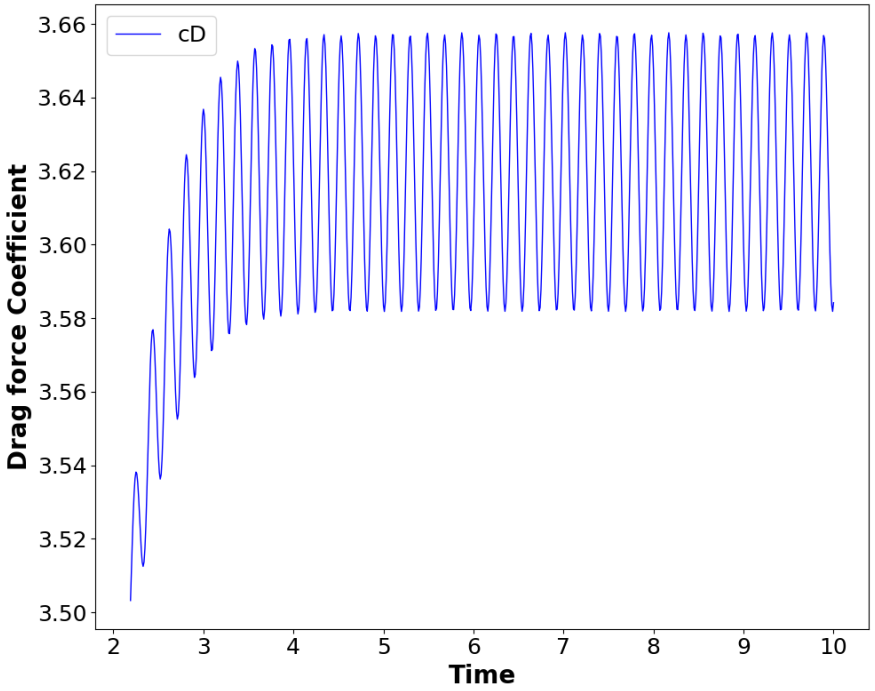

FIGURE 3.3: Time variation of drag coefficient c_D at $Re = 100$.

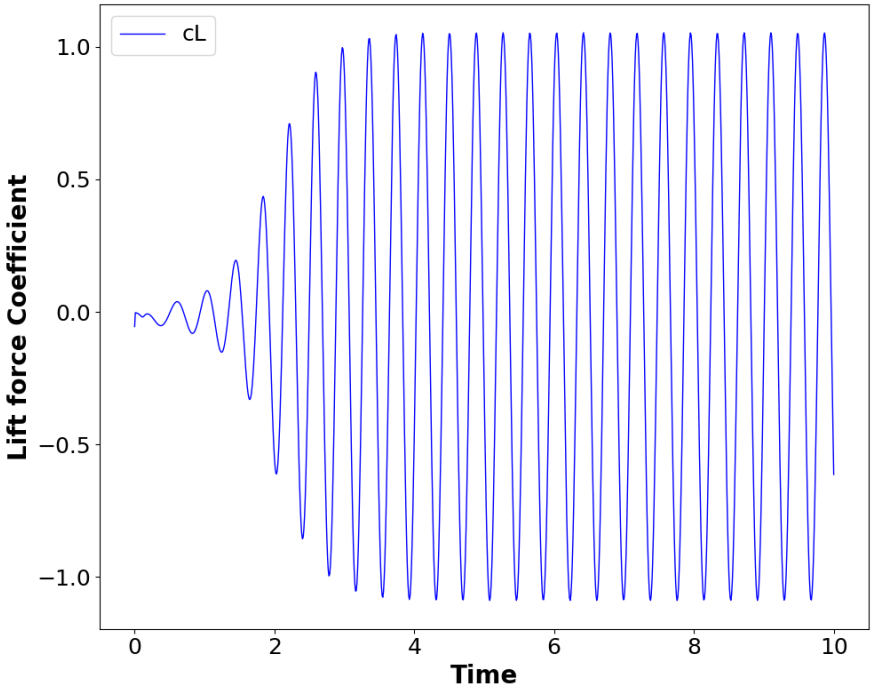

FIGURE 3.4: Time variation of lift coefficient c_L at $Re = 100$.

behind the cylinder. The amplitude of these oscillations remains nearly constant over time, indicating that the flow has reached a stable periodic regime.

In Figure 3.4, the lift coefficient displays a clear sinusoidal pattern after the initial

transient phase. The regularity and uniform amplitude of the oscillations demonstrate that a well-established von Kármán vortex street has developed in the wake. The smoothness of the time signals and absence of high-frequency fluctuations indicate good numerical stability and accuracy of the chosen discretization. The overall amplitude and frequency of both c_D and c_L are consistent with those observed in the benchmark, confirming that the present solver captures the correct unsteady flow characteristics without significant numerical damping or distortion.

3.5.3 Flow Field Evolution with Time

The contours of streamwise velocity U at three representative times are presented in Figure 3.5. These snapshots illustrate the progressive development of the flow field from the initial start-up to the fully established periodic regime.

At the early stage ($t = 1$), the velocity field is mostly attached to the cylinder surface with no visible separation in the wake. As time advances to $t = 5$, the separated shear layers from the cylinder begin to roll up and form vortical structures in the near wake. At $t = 20$, the flow reaches a fully periodic regime where alternate vortices are shed from either side of the cylinder, forming a classical von Kármán vortex street downstream. The wake remains stable and symmetric in its mean structure, which corresponds to the regular oscillations observed in the lift coefficient time-history. The overall flow evolution clearly demonstrates the transition from a steady start-up to a periodic shedding regime, accurately capturing the benchmark flow physics at this Reynolds number.

This chapter has successfully demonstrated the validation of the computational framework against the established Turek and Schäfer benchmark case using conventional numerical methods. The implementation employs the standard Galerkin method for spatial discretization and first-order backward Euler scheme for temporal discretization, providing a robust and computationally efficient approach.

The successful reproduction of this benchmark case at Re = 100 establishes confidence in the numerical methodology and ensures the reliability of subsequent simulations involving more complex physical phenomena.

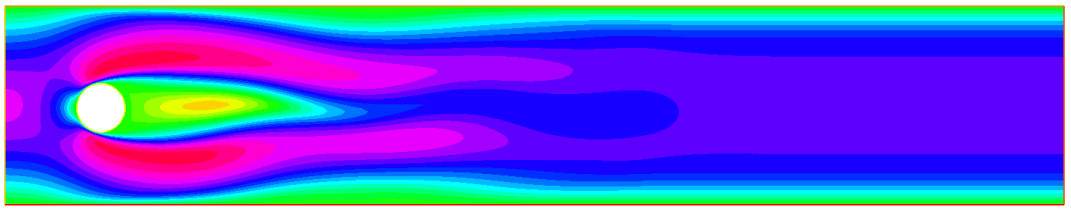

(a) $t = 1$

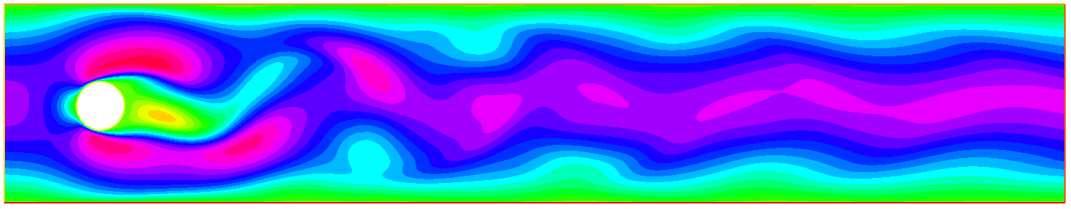

(b) $t = 5$

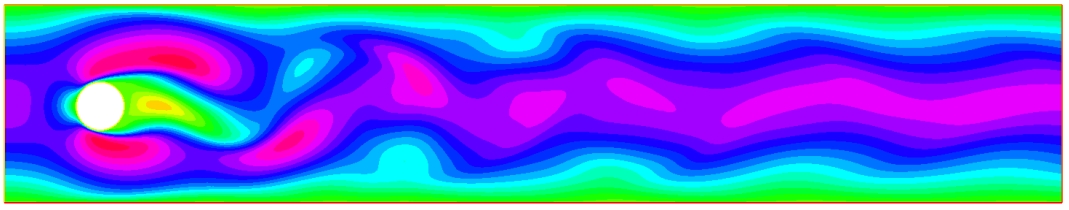

(c) $t = 20$

FIGURE 3.5: Contours of streamwise velocity U at different time instants for $Re = 100$. The color scale represents the magnitude of the streamwise velocity component, ranging from low velocity (dark blue) near solid boundaries and in the wake region to high velocity (red) in the core flow region.

Chapter 4

Numerical Investigation of Radiative Magneto-Micropolar Flow and Heat Transfer in a Channel with Dual Cylinders

4.1 Introduction

Building upon the validated computational framework established in Chapter 3, this chapter presents the core numerical investigation of radiative magneto-micropolar flow and heat transfer in a channel containing two circular cylinders of different diameters arranged in tandem configuration. The study systematically examines the complex interactions between microrotational effects, magnetic fields, and thermal radiation, with particular emphasis on the effects of Eringen's micropolar parameters and magnetic parameters on flow characteristics and thermal performance.

The novel contributions of this chapter include:

i) Development of a comprehensive computational framework for coupled radiative magneto-micropolar flows.

ii) Detailed analysis of wake interference and vortex dynamics in the presence of microrotational and magnetic effects.

iii) Systematic investigation of parameter effects on heat transfer enhancement and flow control.

4.2 Problem Description

4.2.1 Geometrical Configuration

The computational domain consists of a two-dimensional horizontal channel containing two circular cylinders arranged in tandem along the channel centerline, as illustrated in Figure 4.1. The geometry builds upon the validated benchmark case from Chapter 3 while introducing the second cylinder to study wake interference effects.

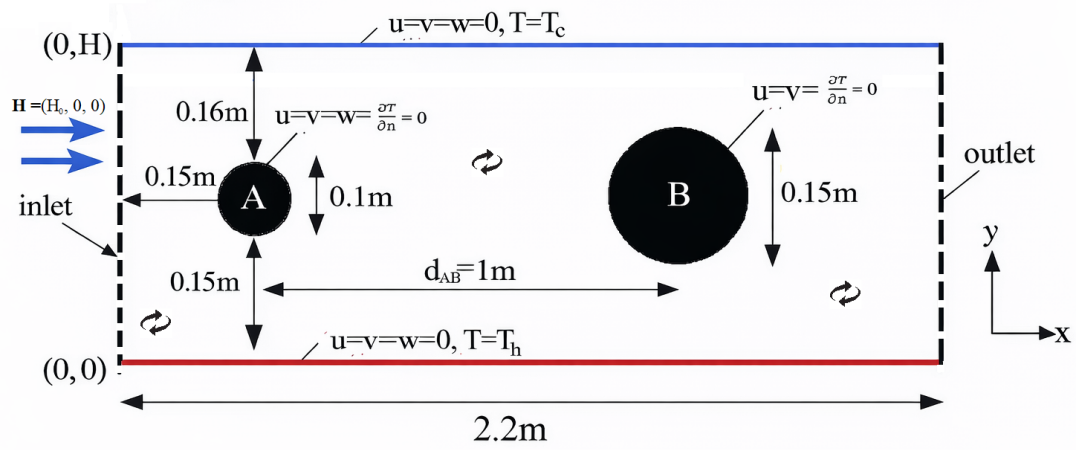

FIGURE 4.1: Computational domain with two cylinders in tandem arrangement. Dimensions: $H = 0.41$ m, $D_A = 0.1$ m, $D_B = 0.15$ m, $d_{AB} = 1.0$ m.

The geometrical parameters are specified as follows:

i) Channel height: $H = 0.41$ m.

ii) Channel length: $L = 2.2$ m.

iii) Cylinder A diameter: $D_A = 0.1$ m.

iv) Cylinder B diameter: $D_B = 0.15$ m.

v) Distance between centers: $d_{AB} = 1.0$ m.

The inter-cylinder spacing of $d_{AB} = 1.0$ m is selected based on preliminary studies indicating significant wake interaction effects at this distance while avoiding complete wake suppression.

4.2.2 Fluid Properties and Reference Parameters

The base fluid properties are maintained consistent with the validation case:

i) Density: $\rho = 1.0$ kg/m^3.

ii) Dynamic viscosity: $\eta = 0.001$ Pa·s.

iii) Thermal conductivity: $\kappa = 0.1$ W/m·K.

iv) Specific heat: $c_p = 1000$ J/kg·K.

v) Mean velocity: $\bar{U} = \frac{2U_{max}}{3}$.

4.3 Mathematical Modeling

This section present the mathematical model of the radiative magneto-micropolar flow and heat transfer model.

4.3.1 Governing Equations

The flow is governed by the following set of radiative magneto-micropolar equations [39]:

$$\nabla \cdot \mathbf{u} = 0, \tag{4.1}$$

$$\rho\left(\frac{\partial \mathbf{u}}{\partial t} + (\mathbf{u}\cdot\nabla)\mathbf{u}\right) = -\nabla p + (\eta + \eta_r)\nabla^2\mathbf{u} + 2\eta_r \nabla \times (\mathbf{W} - \boldsymbol{\omega}) + \mathbf{J} \times \mathbf{B}, \tag{4.2}$$

$$\rho j\left(\frac{\partial \mathbf{W}}{\partial t} + (\mathbf{u}\cdot\nabla)\mathbf{W}\right) = \gamma\nabla^2\mathbf{W} + 4\eta_r(\boldsymbol{\omega} - \mathbf{W}) + \mathbf{M} \times \mathbf{H}, \tag{4.3}$$

$$\rho c_p\left(\frac{\partial T}{\partial t} + (\mathbf{u}\cdot\nabla)T\right) = \kappa\nabla^2 T + \nabla\cdot\mathbf{q}_r + 4\eta_r|\boldsymbol{\omega} - \mathbf{W}|^2 + \tau M_0\frac{|\mathbf{M}\times\mathbf{H}|^2}{|\mathbf{H}|}, \tag{4.4}$$

where ρ is the fluid density, η is the classical dynamic viscosity, and η_r is the microrotational viscosity. The parameter j denotes the micro-inertia density of microelements, while γ is the spin-gradient viscosity. Furthermore, c_p is the specific heat at constant pressure, κ is the thermal conductivity of the fluid, M_0 is the equilibrium magnetization, and τ represents the magnetic relaxation time.

The thermal radiation flux $\mathbf{q}_r$ is modeled using the Rosseland approximation for optically thick media:

$$\mathbf{q}_r = -\frac{16\sigma^* T_c^3}{3\beta_R}\nabla T, \tag{4.5}$$

where, σ^* is the Stefan-Boltzmann constant and β_R is the Rosseland mean absorption coefficient. This formulation leads to an effective radiative conductivity that significantly enhances heat transfer in high-temperature applications. The set of equations (4.1)-(4.4) extends the existing literature by incorporating radiative heat transfer coupled with micromagnetorotative effects. This coupling is significant because both microrotations at the microscale and radiative transport affect

the distribution of thermal flux at the macroscale within the flow channel. The constitutive relation of magnetization is taken as follows [39]:

$$\mathbf{B} = \mu_0 \mathbf{H} + \mathbf{M}, \tag{4.6}$$

where the magnetization vector $\mathbf{M}$, accounting for micro-magnetorotation effects is given as:

$$\mathbf{M} = \frac{M_0(\mathbf{I} - \tau \mathbf{W} \cdot \boldsymbol{\epsilon}) \cdot \mathbf{H}}{|\mathbf{H}|}. \tag{4.7}$$

In the present analysis the state variables are:

$$\mathbf{u} = (u(x,y,t), v(x,y,t), 0), \quad \boldsymbol{\omega} = (0, 0, \omega_z(x,y,t)), \quad \mathbf{W} = (0, 0, w(x,y,t)),$$

where $\mathbf{u}$ and $\mathbf{W}$ are the translational and micro-rotation velocities, respectively, and $\boldsymbol{\omega}$ is the vorticity field $\boldsymbol{\omega} = \frac{1}{2}\nabla \times \mathbf{u}$.

In addition, assume that $\mathbf{H} = (H_0, 0, 0)$. By these simplifications, Eq. (4.7) reduces to:

$$\mathbf{M} = (M_0, -M_0 \tau w, 0). \tag{4.8}$$

The components of the magnetic induction vector in Eq. (4.6) become:

$$B_x = \mu_0 H_0 + M_0, \quad B_y = -\mu_0 M_0 \tau w, \quad B_z = 0. \tag{4.9}$$

Assuming the electric field $\mathbf{E}$ is negligible, Ohm's law yields the current density:

$$\mathbf{J} = \sigma(\mathbf{u} \times \mathbf{B}), \tag{4.10}$$

whose the only z-component is non-zero in the present case and is calculated as:

$$J_z = \sigma(uB_y - vB_x). \tag{4.11}$$

The Lorentz force present in the considered system thus can be expressed as:

$$\mathbf{J} \times \mathbf{B} = (-J_z B_y, J_z B_x, 0). \tag{4.12}$$

The x and y-components of Lorentz force are given by:

$$(\mathbf{J} \times \mathbf{B})_x = -\sigma(uB_y - vB_x)B_y = -\sigma B_y(uB_y - vB_x), \tag{4.13}$$

$$(\mathbf{J} \times \mathbf{B})_y = \sigma(uB_y - vB_x)B_x = \sigma B_x(uB_y - vB_x). \tag{4.14}$$

Similarly, the magnetization torque terms in Eqs. (4.3) and (4.4), reduce to

$$(\mathbf{M} \times \mathbf{H})_z = M_0 \tau H_0 w. \tag{4.15}$$

For the radiation term in the energy equation, considering predominantly transverse radiative heat transfer, we have:

$$\nabla \cdot \mathbf{q}_r = \frac{\partial}{\partial y}\left(\kappa_r \frac{\partial T}{\partial y}\right), \quad \kappa_r = \frac{16\sigma^* T_c^3}{3\beta_R}. \tag{4.16}$$

The system in Eqs. (4.1)-(4.4) thus reduces to the following two-dimensional form:

$$\frac{\partial u}{\partial x} + \frac{\partial v}{\partial y} = 0, \tag{4.17}$$

$$\begin{aligned}\rho\left(\frac{\partial u}{\partial t} + u\frac{\partial u}{\partial x} + v\frac{\partial u}{\partial y}\right) = &-\frac{\partial p}{\partial x} + (\eta + \eta_r)\left(\frac{\partial^2 u}{\partial x^2} + \frac{\partial^2 u}{\partial y^2}\right) \\ &+ \eta_r \frac{\partial}{\partial y}\left(2w - \frac{\partial v}{\partial x} + \frac{\partial u}{\partial y}\right) - \sigma B_y(uB_y - vB_x),\end{aligned} \tag{4.18}$$

$$\begin{aligned}\rho\left(\frac{\partial v}{\partial t} + u\frac{\partial v}{\partial x} + v\frac{\partial v}{\partial y}\right) = &-\frac{\partial p}{\partial y} + (\eta + \eta_r)\left(\frac{\partial^2 v}{\partial x^2} + \frac{\partial^2 v}{\partial y^2}\right) \\ &- \eta_r \frac{\partial}{\partial x}\left(2w - \frac{\partial v}{\partial x} + \frac{\partial u}{\partial y}\right) + \sigma B_x(uB_y - vB_x),\end{aligned} \tag{4.19}$$

$$\rho j\left(\frac{\partial w}{\partial t}+u\frac{\partial w}{\partial x}+v\frac{\partial w}{\partial y}\right)=\gamma\left(\frac{\partial^2 w}{\partial x^2}+\frac{\partial^2 w}{\partial y^2}\right)+2\eta_r\left(\frac{\partial v}{\partial x}-\frac{\partial u}{\partial y}-2w\right)+M_0\tau H_0 w, \tag{4.20}$$

$$\begin{aligned}\rho c_p\left(\frac{\partial T}{\partial t}+u\frac{\partial T}{\partial x}+v\frac{\partial T}{\partial y}\right)=&\kappa\left(\frac{\partial^2 T}{\partial x^2}+\frac{\partial^2 T}{\partial y^2}\right)+\frac{\partial}{\partial y}\left(\kappa_r\frac{\partial T}{\partial y}\right)\\&+\eta_r\left(\frac{\partial v}{\partial x}-\frac{\partial u}{\partial y}-2w\right)^2+H_0(\tau M_0)^3w^2.\end{aligned} \tag{4.21}$$

The associated boundary conditions are given as

$$\begin{cases} u=\dfrac{4U_{\max}y(H-y)}{H^2}, \quad v=0, \quad w=0, \quad \dfrac{\partial T}{\partial x}=0, & \text{at inlet}\\ u=v=w=0, \quad T=T_c, & \text{at upper plate}\\ u=v=w=0, \quad T=T_h, & \text{at lower plate}\\ u=v=w=0, \quad \dfrac{\partial T}{\partial n}=0, & \text{at cylinders}\\ \dfrac{\partial u}{\partial x}=\dfrac{\partial v}{\partial x}=\dfrac{\partial w}{\partial x}=\dfrac{\partial T}{\partial n}=0. & \text{at outlet}\end{cases} \tag{4.22}$$

4.3.2 Non-Dimensionalization

The governing Eqs. (4.17)-(4.21) along with the boundary conditions in Eq. (4.22) are non-dimensionalized with the introduction of the following variables

$$X=\frac{x}{D},\ Y=\frac{y}{D},\ t^*=\frac{\bar{U}}{D}t,\ U=\frac{u}{\bar{U}},\ V=\frac{v}{\bar{U}},\ W=\frac{Dw}{\bar{U}},\ P=\frac{p}{\rho\bar{U}^2},\ \theta=\frac{T-T_c}{T_h-T_c}. \tag{4.23}$$

Substituting Eq. (4.23) into Eqs. (4.17)-(4.21) yields the following non-dimensional system:

$$\frac{\partial U}{\partial X}+\frac{\partial V}{\partial Y}=0, \tag{4.24}$$

$$\frac{\partial U}{\partial t^*} + U\frac{\partial U}{\partial X} + V\frac{\partial U}{\partial Y} = -\frac{\partial P}{\partial X} + \frac{1}{Re}(1+K)\nabla^2 U + \frac{K}{Re}\left(2\frac{\partial W}{\partial Y} - \frac{\partial^2 V}{\partial Y \partial X} + \frac{\partial^2 U}{\partial Y^2}\right) - \beta U W^2 - \alpha V W, \tag{4.25}$$

$$\frac{\partial V}{\partial t^*} + U\frac{\partial V}{\partial X} + V\frac{\partial V}{\partial Y} = -\frac{\partial P}{\partial Y} + \frac{1}{Re}(1+K)\nabla^2 V - \frac{K}{Re}\left(2\frac{\partial W}{\partial X} - \frac{\partial^2 V}{\partial X^2} + \frac{\partial^2 U}{\partial X \partial Y}\right) - \alpha U W - \frac{\alpha^2}{\beta} V, \tag{4.26}$$

$$\frac{\partial W}{\partial t^*} + U\frac{\partial W}{\partial X} + V\frac{\partial W}{\partial Y} = \frac{K_m}{Re}\nabla^2 W + \frac{2K}{Re \cdot Er}\left(\frac{\partial V}{\partial X} - \frac{\partial U}{\partial Y} - 2W\right) + M_s W, \tag{4.27}$$

$$\frac{\partial \theta}{\partial t^*} + U\frac{\partial \theta}{\partial X} + V\frac{\partial \theta}{\partial Y} = \frac{1}{Re \cdot Pr}\left(\frac{\partial^2 \theta}{\partial X^2} + \frac{\partial^2 \theta}{\partial Y^2}\right) + \frac{R_d}{Re \cdot Pr}\frac{\partial^2 \theta}{\partial Y^2} + \frac{K}{Re} Ec \left(\frac{\partial V}{\partial X} - \frac{\partial U}{\partial Y} - 2W\right)^2 + \Gamma W^2. \tag{4.28}$$

In Eqs. (4.25)-(4.28) the parameters Re, K, Er, α, β, M_s, Γ, Ec, Pr, K_m, and R_d are defined respectively as:

$$Re = \frac{\rho \bar{U} D}{\eta}, \quad K = \frac{\eta_r}{\eta}, \quad Er = \frac{j}{D^2}, \quad \alpha = \frac{\sigma\, \mu_0\, \tau M_0\, (H_0 + M_0)}{\rho}, \quad \beta = \frac{\sigma \bar{U}\, \tau^2 M_0^2}{\rho D},$$
$$M_s = \frac{M_0 \tau H_0 D}{\rho j \bar{U}}, \quad \Gamma = \frac{\tau^3 M_0^3 H_0 \bar{U}}{\rho c_p (T_h - T_c) D}, \quad Ec = \frac{\bar{U}^2}{c_p (T_h - T_c)},$$
$$Pr = \frac{\eta c_p}{\kappa}, \quad K_m = \frac{\gamma}{\eta j}, \quad R_d = \frac{\kappa_r}{\kappa} = \frac{16 \sigma^* T_c^3}{3 \beta_R \kappa}. \tag{4.29}$$

These dimensionless numbers characterize the relative importance of inertial, micropolar, magnetic, and thermal effects in the flow. The radiation parameter R_d

represents the relative importance of radiative to conductive heat transfer, with larger values indicating stronger radiative effects.

Likewise, the boundary conditions in Eq. (4.22) are transformed into the following form:

$$\begin{cases} U = \dfrac{4U_{\max}Y(H-Y)}{H^2}, \quad V = 0, \quad W = 0, \quad \dfrac{\partial\theta}{\partial X} = 0 & \text{at the inlet,} \\ U = V = W = 0, \quad \theta = 0 & \text{at the upper plate,} \\ U = V = W = 0, \quad \theta = 1 & \text{at the lower plate,} \\ U = V = W = 0, \quad \dfrac{\partial\theta}{\partial n} = 0 & \text{at the cylinders,} \\ \dfrac{\partial U}{\partial X} = \dfrac{\partial V}{\partial X} = \dfrac{\partial W}{\partial X} = \dfrac{\partial\theta}{\partial X} = 0 & \text{at the outlet.} \end{cases} \tag{4.30}$$

4.4 Weak Formulation of the Problem

To define the weak form of the problem in Eqs. (4.24)-(4.28) we consider the triangulation of the computational domain Ω as shown in Fig. 4.2. The finite-element approximation employs Taylor-Hood ($P2$-$P1$) elements for velocity and pressure, and $P2$ elements for microrotation and temperature.

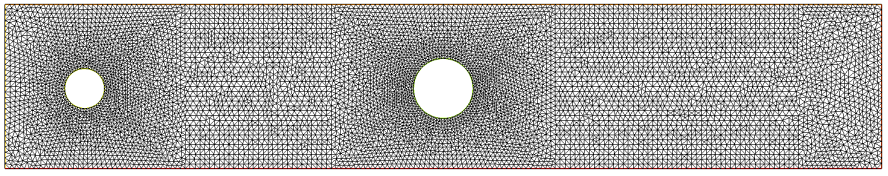

FIGURE 4.2: Triangulated computational domain with local refinement around cylinders with 5840 elements .

We define the following finite-dimensional finite element spaces:

$$\begin{aligned} \mathcal{U}_h &= \left\{ \mathbf{u}_h \in \left(H_0^1(\Omega)\right)^2 \;\middle|\; \mathbf{u}_h|_K \in (P_2(K))^2,\ \forall K \in \Omega_h \right\}, \\ \mathcal{P}_h &= \left\{ p_h \in L^2(\Omega) \;\middle|\; p_h|_K \in P_1(K),\ \forall K \in \Omega_h \right\}, \\ \mathcal{W}_h &= \left\{ w_h \in H_0^1(\Omega) \;\middle|\; w_h|_K \in P_2(K),\ \forall K \in \Omega_h \right\}, \\ \mathcal{T}_h &= \left\{ \theta_h \in H^1(\Omega) \;\middle|\; \theta_h|_K \in P_2(K),\ \forall K \in \Omega_h \right\}. \end{aligned} \tag{4.31}$$

The weak form is obtained by multiplying the governing equations by test functions $(\tilde{\mathbf{u}}, \tilde{p}, \tilde{w}, \tilde{\theta})$ from the corresponding function spaces, integrating over the domain, and applying integration by parts. The resulting variational problem is to find $(\mathbf{u}, p, w, \theta) \in \mathcal{U}_h \times \mathcal{P}_h \times \mathcal{W}_h \times \mathcal{T}_h$ such that for all test functions $(\tilde{\mathbf{u}}, \tilde{p}, \tilde{w}, \tilde{\theta})$:

$$\int_\Omega \tilde{p}\left(\frac{\partial U}{\partial X}+\frac{\partial V}{\partial Y}\right)d\Omega = 0, \tag{4.32}$$

$$\begin{aligned}
&\int_\Omega \tilde{U}\frac{\partial U}{\partial t^*}d\Omega+\int_\Omega \tilde{U}\left(U\frac{\partial U}{\partial X}+V\frac{\partial U}{\partial Y}\right)d\Omega+\frac{1}{Re}(1+K)\int_\Omega\left(\frac{\partial \tilde{U}}{\partial X}\frac{\partial U}{\partial X}+\frac{\partial \tilde{U}}{\partial Y}\frac{\partial U}{\partial Y}\right)d\Omega\\
&\quad-\frac{K}{Re}\int_\Omega\left[\frac{\partial \tilde{U}}{\partial Y}\left(\frac{\partial V}{\partial X}-\frac{\partial U}{\partial Y}\right)-2W\frac{\partial \tilde{U}}{\partial Y}\right]d\Omega+\int_\Omega\left(\beta UW^2+\alpha VW\right)\tilde{U}d\Omega\\
&-\int_\Omega P\frac{\partial \tilde{U}}{\partial X}d\Omega=\int_{\partial\Omega}\tilde{U}\left(\frac{1}{Re}\frac{\partial U}{\partial n}+\frac{K}{Re}\left(-\frac{\partial V}{\partial X}n_y+\frac{\partial U}{\partial Y}n_y+2Wn_y\right)-Pn_x\right)ds,
\end{aligned} \tag{4.33}$$

$$\begin{aligned}
&\int_\Omega \tilde{V}\frac{\partial V}{\partial t^*}d\Omega+\int_\Omega \tilde{V}\left(U\frac{\partial V}{\partial X}+V\frac{\partial V}{\partial Y}\right)d\Omega+\frac{1}{Re}(1+K)\int_\Omega\left(\frac{\partial \tilde{V}}{\partial X}\frac{\partial V}{\partial X}+\frac{\partial \tilde{V}}{\partial Y}\frac{\partial V}{\partial Y}\right)d\Omega\\
&\quad+\frac{K}{Re}\int_\Omega\left[\frac{\partial \tilde{V}}{\partial X}\left(\frac{\partial V}{\partial X}-\frac{\partial U}{\partial Y}\right)-2W\frac{\partial \tilde{V}}{\partial X}\right]d\Omega+\int_\Omega\left(\alpha UW+\frac{\alpha^2}{\beta}V\right)\tilde{V}d\Omega\\
&-\int_\Omega P\frac{\partial \tilde{V}}{\partial Y}d\Omega=\int_{\partial\Omega}\tilde{V}\left(\frac{1}{Re}\frac{\partial V}{\partial n}-\frac{K}{Re}\left(-\frac{\partial V}{\partial X}n_x+\frac{\partial U}{\partial Y}n_x+2Wn_x\right)-Pn_y\right)ds,
\end{aligned} \tag{4.34}$$

$$\begin{aligned}
&\int_\Omega \tilde{W}\frac{\partial W}{\partial t^*}d\Omega+\int_\Omega \tilde{W}\left(U\frac{\partial W}{\partial X}+V\frac{\partial W}{\partial Y}\right)d\Omega+\frac{K_m}{Re}\int_\Omega\left(\frac{\partial \tilde{W}}{\partial X}\frac{\partial W}{\partial X}+\frac{\partial \tilde{W}}{\partial Y}\frac{\partial W}{\partial Y}\right)d\Omega\\
&-\frac{2K}{Re\cdot Er}\int_\Omega \tilde{W}\left(\frac{\partial V}{\partial X}-\frac{\partial U}{\partial Y}-2W\right)d\Omega-M_s\int_\Omega \tilde{W}Wd\Omega=\frac{K_m}{Re}\int_{\partial\Omega}\tilde{W}\frac{\partial W}{\partial n}ds,
\end{aligned} \tag{4.35}$$

$$\int_\Omega \tilde{\theta}\frac{\partial\theta}{\partial t^*}d\Omega + \int_\Omega \tilde{\theta}\left(U\frac{\partial\theta}{\partial X} + V\frac{\partial\theta}{\partial Y}\right)d\Omega + \frac{1}{Re\cdot Pr}\int_\Omega\left(\frac{\partial\tilde{\theta}}{\partial X}\frac{\partial\theta}{\partial X} + \frac{\partial\tilde{\theta}}{\partial Y}\frac{\partial\theta}{\partial Y}\right)d\Omega$$
$$+ \frac{R_d}{Re\cdot Pr}\int_\Omega \frac{\partial\tilde{\theta}}{\partial Y}\frac{\partial\theta}{\partial Y}d\Omega - \int_\Omega\left[\frac{K}{Re}Ec\left(\frac{\partial V}{\partial X} - \frac{\partial U}{\partial Y} - 2W\right)^2 + \Gamma W^2\right]\tilde{\theta}d\Omega$$
$$= \frac{1}{Re\cdot Pr}\int_{\partial\Omega}\tilde{\theta}\left(\frac{\partial\theta}{\partial X}n_X + \frac{\partial\theta}{\partial Y}n_Y\right)ds + \frac{R_d}{Re\cdot Pr}\int_{\partial\Omega}\tilde{\theta}\frac{\partial\theta}{\partial Y}n_Y ds. \quad (4.36)$$

4.4.1 Time Discretization

The system of equations is discretized in time using the first-order backward Euler method. For a generic variable ϕ, the time derivative is approximated as:

$$\frac{\partial\phi}{\partial t^*} \approx \frac{\phi^{n+1} - \phi^n}{\Delta t^*}, \quad (4.37)$$

where, Δt^* is the non-dimensional time step, and superscripts denote the time level. The variational problem at time level t^{n+1} is to find $(U^{n+1}, V^{n+1}, P^{n+1}, W^{n+1}, \theta^{n+1})$ defined on the domain Ω^{n+1} such that the following equations are satisfied for all admissible test functions.

$$\int_{\Omega^{n+1}}\tilde{p}\left(\frac{\partial U^{n+1}}{\partial X^{n+1}} + \frac{\partial V^{n+1}}{\partial Y^{n+1}}\right)d\Omega = 0, \quad \forall\tilde{p}\in\mathcal{P}_h. \quad (4.38)$$

$$\frac{1}{\Delta t^*}\int_{\Omega^{n+1}}\left(U^{n+1} - U^n\right)\tilde{U}\,d\Omega + \int_{\Omega^{n+1}}\left(U^n\frac{\partial U^{n+1}}{\partial X^{n+1}} + V^n\frac{\partial U^{n+1}}{\partial Y^{n+1}}\right)\tilde{U}\,d\Omega$$
$$+ \frac{1+K}{Re}\int_{\Omega^{n+1}}\left(\frac{\partial U^{n+1}}{\partial X^{n+1}}\frac{\partial\tilde{U}}{\partial X^{n+1}} + \frac{\partial U^{n+1}}{\partial Y^{n+1}}\frac{\partial\tilde{U}}{\partial Y^{n+1}}\right)d\Omega$$
$$- \frac{K}{Re}\int_{\Omega^{n+1}}\left[\frac{\partial V^{n+1}}{\partial X^{n+1}}\frac{\partial\tilde{U}}{\partial Y^{n+1}} - \frac{\partial U^{n+1}}{\partial Y^{n+1}}\frac{\partial\tilde{U}}{\partial Y^{n+1}} - 2W^{n+1}\frac{\partial\tilde{U}}{\partial Y^{n+1}}\right]d\Omega$$
$$+ \int_{\Omega^{n+1}}\left(\beta U^{n+1}(W^{n+1})^2 + \alpha V^{n+1}W^{n+1}\right)\tilde{U}\,d\Omega$$
$$- \int_{\Omega^{n+1}}P^{n+1}\frac{\partial\tilde{U}}{\partial X^{n+1}}\,d\Omega = 0, \quad \forall\tilde{U}\in\mathcal{U}_h. \quad (4.39)$$

$$\frac{1}{\Delta t^*}\int_{\Omega^{n+1}}\left(V^{n+1}-V^n\right)\tilde{V}\,d\Omega+\int_{\Omega^{n+1}}\left(U^n\frac{\partial V^{n+1}}{\partial X^{n+1}}+V^n\frac{\partial V^{n+1}}{\partial Y^{n+1}}\right)\tilde{V}\,d\Omega$$
$$+\frac{1+K}{Re}\int_{\Omega^{n+1}}\left(\frac{\partial V^{n+1}}{\partial X^{n+1}}\frac{\partial \tilde{V}}{\partial X^{n+1}}+\frac{\partial V^{n+1}}{\partial Y^{n+1}}\frac{\partial \tilde{V}}{\partial Y^{n+1}}\right)d\Omega$$
$$+\frac{K}{Re}\int_{\Omega^{n+1}}\left[\frac{\partial V^{n+1}}{\partial X^{n+1}}\frac{\partial \tilde{V}}{\partial X^{n+1}}-\frac{\partial U^{n+1}}{\partial Y^{n+1}}\frac{\partial \tilde{V}}{\partial X^{n+1}}-2W^{n+1}\frac{\partial \tilde{V}}{\partial X^{n+1}}\right]d\Omega$$
$$+\int_{\Omega^{n+1}}\left(\alpha U^{n+1}W^{n+1}+\frac{\alpha^2}{\beta}V^{n+1}\right)\tilde{V}\,d\Omega$$
$$-\int_{\Omega^{n+1}}P^{n+1}\frac{\partial \tilde{V}}{\partial Y^{n+1}}\,d\Omega=0,\quad\forall\tilde{V}\in\mathcal{U}_h.\quad(4.40)$$

$$\frac{1}{\Delta t^*}\int_{\Omega^{n+1}}\left(W^{n+1}-W^n\right)\tilde{W}\,d\Omega+\int_{\Omega^{n+1}}\left(U^n\frac{\partial W^{n+1}}{\partial X^{n+1}}+V^n\frac{\partial W^{n+1}}{\partial Y^{n+1}}\right)\tilde{W}\,d\Omega$$
$$+\frac{K_m}{Re}\int_{\Omega^{n+1}}\left(\frac{\partial W^{n+1}}{\partial X^{n+1}}\frac{\partial \tilde{W}}{\partial X^{n+1}}+\frac{\partial W^{n+1}}{\partial Y^{n+1}}\frac{\partial \tilde{W}}{\partial Y^{n+1}}\right)d\Omega$$
$$-\frac{2K}{Re\cdot Er}\int_{\Omega^{n+1}}\left(\frac{\partial V^{n+1}}{\partial X^{n+1}}-\frac{\partial U^{n+1}}{\partial Y^{n+1}}-2W^{n+1}\right)\tilde{W}\,d\Omega$$
$$-M_s\int_{\Omega^{n+1}}W^{n+1}\tilde{W}\,d\Omega=0,\quad\forall\tilde{W}\in\mathcal{W}_h.\quad(4.41)$$

$$\frac{1}{\Delta t^*}\int_{\Omega^{n+1}}\left(\theta^{n+1}-\theta^n\right)\tilde{\theta}\,d\Omega+\int_{\Omega^{n+1}}\left(U^n\frac{\partial \theta^{n+1}}{\partial X^{n+1}}+V^n\frac{\partial \theta^{n+1}}{\partial Y^{n+1}}\right)\tilde{\theta}\,d\Omega$$
$$+\frac{1}{Re\cdot Pr}\int_{\Omega^{n+1}}\left(\frac{\partial \theta^{n+1}}{\partial X^{n+1}}\frac{\partial \tilde{\theta}}{\partial X^{n+1}}+\frac{\partial \theta^{n+1}}{\partial Y^{n+1}}\frac{\partial \tilde{\theta}}{\partial Y^{n+1}}\right)d\Omega$$
$$+\frac{R_d}{Re\cdot Pr}\int_{\Omega^{n+1}}\frac{\partial \theta^{n+1}}{\partial Y^{n+1}}\frac{\partial \tilde{\theta}}{\partial Y^{n+1}}\,d\Omega$$
$$-\frac{K}{Re}Ec\int_{\Omega^{n+1}}\left(\frac{\partial V^{n+1}}{\partial X^{n+1}}-\frac{\partial U^{n+1}}{\partial Y^{n+1}}-2W^{n+1}\right)^2\tilde{\theta}\,d\Omega$$
$$-\Gamma\int_{\Omega^{n+1}}\left(W^{n+1}\right)^2\tilde{\theta}\,d\Omega=0,\quad\forall\tilde{\theta}\in\mathcal{T}_h.\quad(4.42)$$

Subjected to following boundary conditions at time t^{n+1}.

i) Dirichlet Boundaries (Γ_D):

$$\text{Inlet } (X=0): \quad U^{n+1} = \frac{4U_m Y(H-Y)}{H^2}, \quad V^{n+1} = 0, \quad W^{n+1} = 0.$$

$$\text{Channel Walls } (Y=0, H): \quad U^{n+1} = 0, \quad V^{n+1} = 0, \quad W^{n+1} = 0.$$

$$\text{Cylinder Surfaces:} \quad U^{n+1} = 0, \quad V^{n+1} = 0, \quad W^{n+1} = 0.$$

$$\text{Temperature Boundaries:} \quad \theta^{n+1} = 1 \text{ at } Y = 0, \quad \theta^{n+1} = 0 \text{ at } Y = H.$$

ii) Neumann Boundaries (Γ_N):

$$\text{Outlet } (X=L): \quad \frac{\partial U^{n+1}}{\partial X} = 0, \quad \frac{\partial V^{n+1}}{\partial X} = 0, \quad \frac{\partial W^{n+1}}{\partial X} = 0,$$

$$\text{Thermal Insulation:} \quad \frac{\partial \theta^{n+1}}{\partial n} = 0 \text{ at inlet, cylinders, and outlet.}$$

4.4.2 Solution Algorithm at Each Time Step

The computational algorithm for advancing from time level n to $n+1$ is as follows:

i) Start with the known solution at time n: $(U^n, V^n, P^n, W^n, \theta^n)$.

ii) Solve the coupled system of equations (4.38), (4.39), and (4.40) for $(U^{n+1}, V^{n+1}, P^{n+1})$ using the previous microrotation field W^n.

iii) Solve equation (4.41) for W^{n+1} using the updated velocity field (U^{n+1}, V^{n+1}).

iv) Solve equation (4.42) for θ^{n+1} using all updated variables $(U^{n+1}, V^{n+1}, W^{n+1})$.

v) Update the solution variables,

$$U^n \leftarrow U^{n+1}, \quad V^n \leftarrow V^{n+1}, \quad P^n \leftarrow P^{n+1}, \quad W^n \leftarrow W^{n+1}, \quad \theta^n \leftarrow \theta^{n+1},$$
$$n \leftarrow n+1.$$

This iterative procedure continues until the total simulation time is reached. The linear system arising from the finite element discretization is solved using appropriate LU factorization method with in FreeFEM++.

4.5 Results and Discussion

This section presents and discusses the numerical results obtained from the simulation of radiative magneto-micropolar flow and heat transfer in a channel containing dual cylinders arranged in tandem. The analysis is carried out using the finite element formulation and numerical scheme described in the previous section. The computed results are presented in both graphical and tabular forms to illustrate the effects of various governing parameters on the flow and thermal fields.

The simulations have been performed for a wide range of dimensionless parameters to explore their individual and combined influences on the overall flow characteristics. The considered parameters include the Reynolds number (Re), micropolar coupling parameter (K), Eringen number (Er), Prandtl number (Pr), Eckert number (Ec), radiation parameter (Rd), magnetic parameter (M_s), and Magnetization dissipation parameter (Γ). Unless otherwise stated, the reference values of the parameters are taken as: $Re = 200$, $K = 0.1$, $Er = 0.1$, $Pr = 0.1$, $Ec = 0.1$, $Rd = 0.1$, $M_s = 0.1$, $\Gamma = 0.5$.
Each parameter is varied systematically within its physical range while keeping the others fixed at the above reference values to analyze its effect on the streamwise velocity, microrotation, and temperature fields. The results are discussed in detail in the following subsections, emphasizing the physical interpretations and trends observed from the computed data.

4.5.1 Parametric Analysis at Drag and Lift coefficient

Tables 4.1 and 4.2 present the computed hydrodynamic and thermal quantities at time $t = 2$ for a range of dimensionless flow parameters. The analysis focuses on the combined effects of the Reynold number (Re), micropolar coupling parameter (K), Eringen number (Er), Prandtl number (Pr), Eckert number (Ec), radiation parameter (Rd), magnetic parameter (M_s), magnetic orientation parameters (α, β), and Magnetization dissipation parameter (Γ) on the flow characteristics and heat transfer behavior within the channel containing dual cylinders.

From Table 4.1, it can be observed that the drag coefficient (c_D) and lift coefficient (c_L) on both cylinders vary noticeably with changes in Re, K, and Er. At lower Reynolds numbers, higher viscous effects lead to larger drag forces, while an increase in Re reduces viscous dominance and enhances inertial effects, slightly decreasing c_D on both cylinders.

TABLE 4.1: Computed drag and lift coefficients at $t = 2$ for different flow parameters.

Re	K	Er	Pr	Ec	Rd	M_s	α	β	Γ	c_{DA}	c_{LA}	c_{DB}	c_{LB}
200	0.001	0.01	0.05	0.01	0.01	0.1	1	1.5	0.1	3.9323	0.001186	4.29545	0.0108238
300										3.38973	0.194009	3.39064	-0.707993
400	0.001									3.45738	-0.716829	3.64139	1.06729
	0.01									3.4585	-0.705722	3.65445	1.13084
	0.1	0.01								3.48224	-0.562755	3.90156	1.44294
		0.05								3.47382	-0.611123	3.76124	1.29767
		0.1	0.05							3.47346	-0.610988	3.75241	1.26398
			0.1							3.47346	-0.610988	3.75241	1.26398
			0.5	0.01						3.47346	-0.610988	3.75241	1.26398
				0.05						3.47346	-0.610988	3.75241	1.26398
				0.1	0.01					3.47346	-0.610988	3.75241	1.26398
					0.05					3.47346	-0.610988	3.75241	1.26398
					0.1	0.1				3.47346	-0.610988	3.75241	1.26398
						0.5				3.47348	-0.61104	3.75282	1.2659
						1	1			3.4735	-0.61112	3.75341	1.2686
							1.5			3.44756	-0.484635	3.68445	1.01225
							2	1.5		3.42758	-0.113941	3.44385	0.66873
								2		3.43519	-0.299237	3.57325	0.901294
								2.5	0.1	3.44289	-0.410658	3.64163	0.999739
									0.5	3.44289	-0.410658	3.64163	0.999739
									1.0	3.44289	-0.410658	3.64163	0.999739

The influence of the micropolar parameter K shows that higher values of K strengthen the coupling between translational and microrotational motions, thereby altering the pressure and velocity gradients around the cylinders. The variation of Er affects the rotational inertia of microelements, modifying the torque and the resulting lift fluctuations on both cylinders. Similarly, parameters such as Pr, Ec,

and Rd affect the flow through their influence on thermal transport and viscous dissipation, which indirectly influence drag and lift forces.

4.5.2 Parametric Analysis at Fixed Point

TABLE 4.2: Computed flow variables at $(x, y) = (0.6, 0.2)$ and $t = 2$ for different flow parameters.

Re	K	Er	Pr	Ec	Rd	M_s	α	β	Γ	U	V	W	θ	ψ
200	0.001	0.01	0.05	0.01	0.01	0.1	1	1.5	0.1	1.03912	0.009696	0.0002366	0.514913	0.237272
300										0.848501	-0.533943	0.0010469	0.504768	0.37522
400	0.001									2.35878	1.48087	0.0001327	0.561355	0.422936
	0.01									2.36063	1.46247	0.0029625	0.562971	0.425048
	0.1	0.01								2.73324	1.15541	0.123102	0.604994	0.469293
		0.05								2.07258	1.46962	-0.016017	0.549673	0.42094
		0.1	0.05							2.04645	1.47507	-0.012296	0.545989	0.417714
			0.1							2.04645	1.47507	-0.012296	0.485098	0.417714
			0.5	0.01						2.04645	1.47507	-0.012296	0.116459	0.417714
				0.05						2.04645	1.47507	-0.012296	0.141158	0.417714
				0.1	0.01					2.04645	1.47507	-0.012296	0.172033	0.417714
					0.05					2.04645	1.47507	-0.012296	0.179703	0.417714
					0.1	0.1				2.04645	1.47507	-0.012296	0.189233	0.417714
						0.5				2.04754	1.47497	-0.012739	0.18937	0.417841
						1	1			2.04909	1.47481	-0.01327	0.189564	0.41802
							1.5			1.80677	1.15922	-0.055587	0.166039	0.394398
							2	1.5		2.29811	-0.294667	-0.057648	0.145485	0.379756
								2		2.0974	0.268193	-0.070543	0.154897	0.373334
								2.5	0.1	1.95381	0.720222	-0.070928	0.159283	0.378097
									0.5	1.95381	0.720222	-0.070928	0.159446	0.378097
									1.0	1.95381	0.720222	-0.070928	0.159651	0.378097

Table 4.2 summarizes the corresponding local flow variables, including the velocity components (U, V), microrotation (W), temperature (θ), and stream function (ψ). The results reveal that as Re increases, the streamwise velocity component U becomes dominant, and recirculation intensity grows near the downstream cylinder. The microrotation component W exhibits sensitive dependence on both K and Er, confirming the strong influence of microstructure and spin effects in the near-wall region. The temperature Θ generally decreases with higher Re and Pr, indicating enhanced convective heat transport, while higher Ec and Rd contribute

to elevated temperature levels due to viscous dissipation and radiative heating. The stream function Ψ reflects the modification of the flow topology in the wake region, showing smoother transitions for higher magnetic and micropolar effects.

The streamwise velocity U at the monitoring point increases by approximately fifteen percent when Re is raised from 200 to 400, while the microrotation W shows a fourfold increase over the same range, highlighting the strong coupling between inertia and rotational motion. Temperature variations are most pronounced with changes in Rd and Γ, where increases of fifty percent in these parameters lead to temperature rises of up to twenty percent. These quantitative trends establish clear correlations between input parameters and output performance metrics, providing valuable design data for engineering applications involving magneto-micropolar flow

4.5.3 Impacts of Reynolds Number

Figures 4.3–4.5 illustrate the influence of the Reynold number on the streamwise velocity, microrotation, and temperature distributions within the channel containing dual cylinders arranged in tandem. The Reynolds number represents the ratio of inertial to viscous forces; hence, its variation significantly alters the flow topology, vortex formation, and heat transfer characteristics. In Figure 4.3, the contours of the streamwise velocity U are plotted for $Re = 100$, 200, 300, and 400.

It is observed that for the lowest Reynold number ($Re = 100$, Figure 4.3(a)), the flow remains largely laminar and attached to the cylinder surfaces, showing only a small recirculation zone behind the downstream cylinder. As Re increases to 200 (Figure 4.3(b)), the velocity gradient near the walls intensifies, and the recirculation bubble becomes more distinct, extending slightly downstream. At $Re = 300$ (Figure 4.3(c)), a pronounced wake region forms, indicating stronger flow separation and increased inertial effects. The flow accelerates between the cylinders, showing a jet-like structure due to the reduced viscous resistance. For the highest Reynolds number ($Re = 400$, Figure 4.3(d)), the streamwise velocity exhibits a larger separated zone and a narrower high-speed core, representing

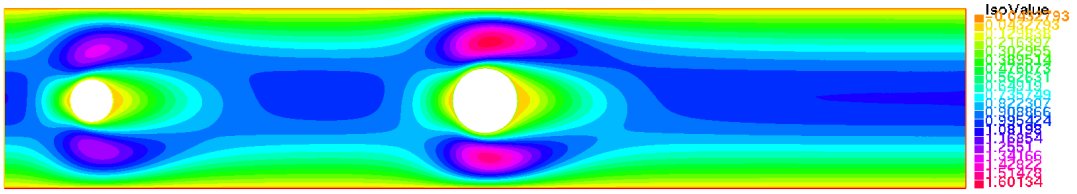

(a) $Re = 100$

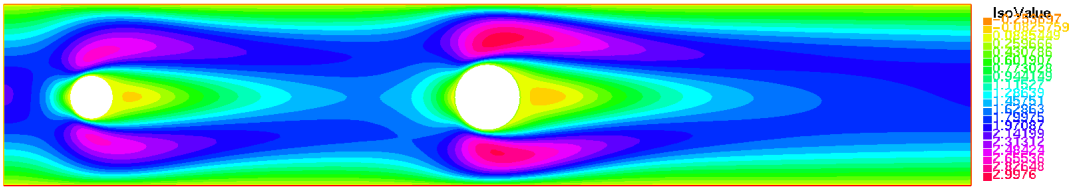

(b) $Re = 200$

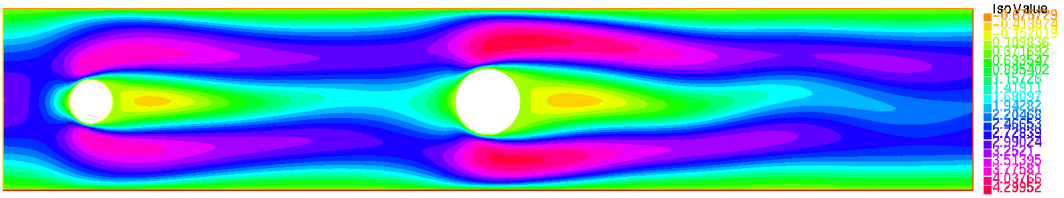

(c) $Re = 300$

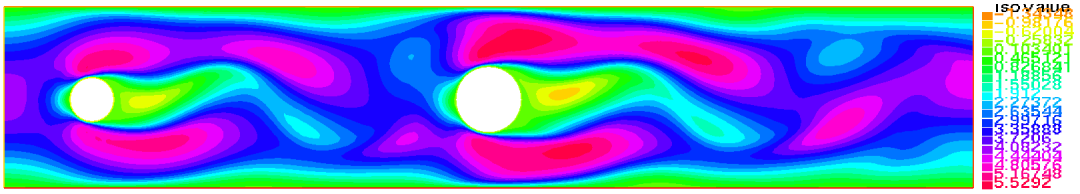

(d) $Re = 400$

FIGURE 4.3: Contours of streamwise velocity (U) for varying Reynolds numbers ($Re = 100$–400). As Re increases, the flow separation and recirculation zones become more pronounced. Parameters: $K = 0.1$, $Er = 0.1$, $Pr = 0.1$, $Ec = 0.1$, $Rd = 0.1$, $Ms = 0.1$, $\alpha = 1$, $\beta = 2$, $\Gamma = 0.5$.

the dominance of inertial effects and thinner boundary layers. Overall, higher Re values enhance the convective transport and flow instability, leading to the elongation of recirculation zones behind both cylinders.

Figure 4.4 presents the microrotation velocity W contours for the same set of Re values. It can be seen that at $Re = 100$ (Figure 4.4(a)), the microrotation remains confined near the solid boundaries, with small magnitude indicating weak spin of the microelements. Increasing Re to 200 (Figure 4.4(b)) enhances the microrotation region behind the cylinders and around the cylinder surfaces due to stronger velocity gradients. For $Re = 300$ and 400 (Figures 4.4(c) and 4.4(d)), the

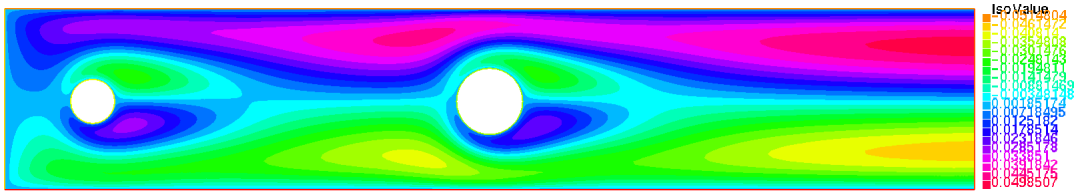

(a) $Re = 100$

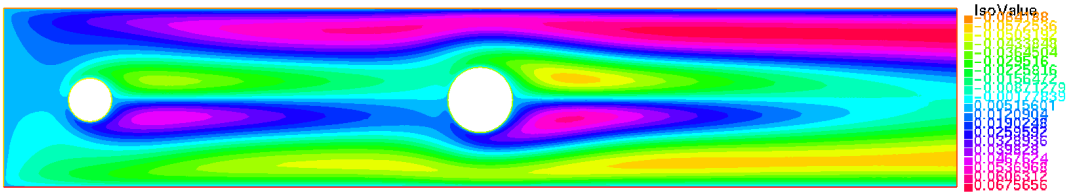

(b) $Re = 200$

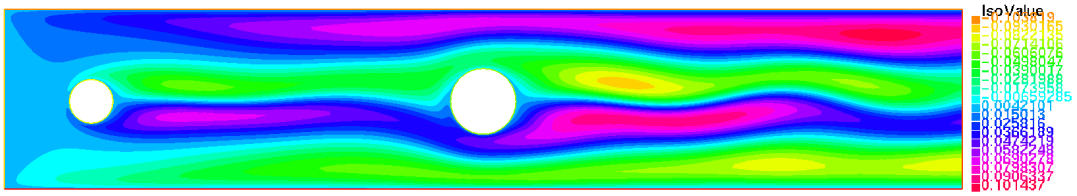

(c) $Re = 300$

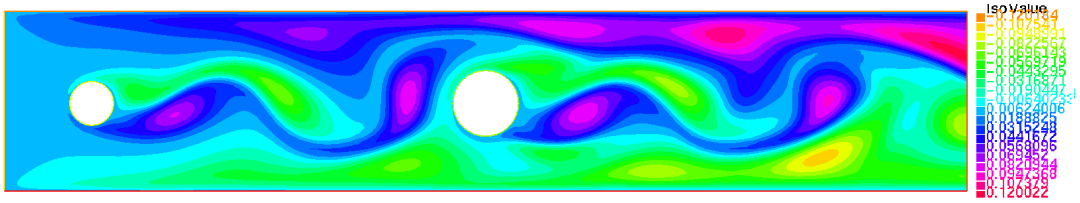

(d) $Re = 400$

FIGURE 4.4: Contours of microrotation velocity W for different Reynold number ($Re = 100$–400). Higher Reynold number enhance rotational motion near the cylinder surfaces and in the wake region, showing the effect of inertia on micro-rotation dynamics. Parameters: $K = 0.1$, $Er = 0.1$, $Pr = 0.1$, $Ec = 0.1$, $Rd = 0.1$, $Ms = 0.1$, $\alpha = 1$, $\beta = 2$, $\Gamma = 0.5$.

microrotation zones expand significantly, particularly in the wake region, revealing that higher inertial forces intensify rotational motion. The results clearly indicate that as inertia dominates over viscous effects, the microrotation field becomes more energetic, demonstrating the strong coupling between microstructure and macroscopic flow behavior.

In Figure 4.5, the temperature contours are shown for varying Re. It can be seen at $Re = 100$ (Figure 4.5(a)), the temperature field shows a thick thermal boundary layer near the cylinder surfaces, implying that heat transfer is mainly

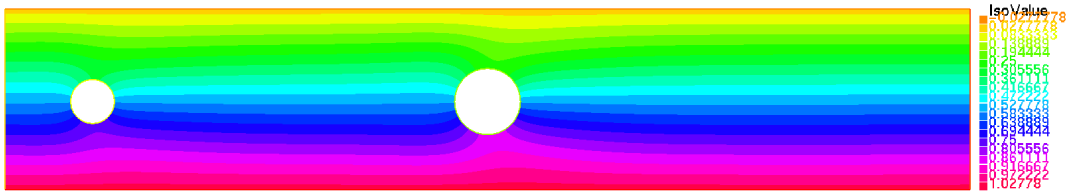

(a) $Re = 100$

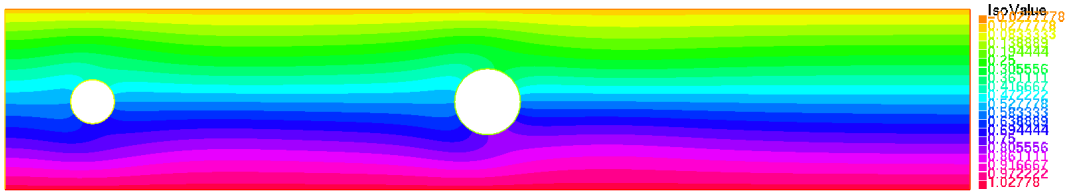

(b) $Re = 200$

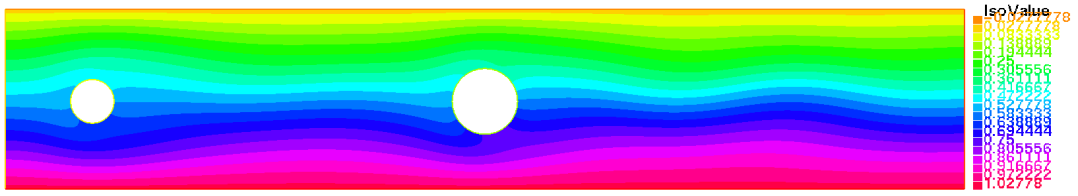

(c) $Re = 300$

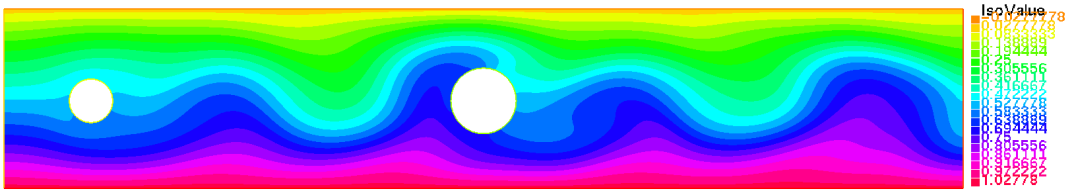

(d) $Re = 400$

FIGURE 4.5: Temperature contours θ for various Reynolds numbers (Re = 100–400). The results show reduced thermal boundary layer thickness and enhanced convective transport as Re increases. Parameters: $K = 0.1$, $Er = 0.1$, $Pr = 0.1$, $Ec = 0.1$, $Rd = 0.1$, $Ms = 0.1$, $\alpha = 1$, $\beta = 2$, $\Gamma = 0.5$.

by conduction. For $Re = 200$ (Figure 4.5(b)), the boundary layer becomes thinner and convective effects start to dominate. At $Re = 300$ (Figure 4.5(c)), the temperature gradients near the surfaces are steeper, leading to enhanced heat removal from the cylinder surface. At the highest Reynolds number ($Re = 400$, Figure 4.5(d)), the boundary layer is extremely thin, and temperature contours align closely with the flow streamlines, showing strong convective transport and efficient thermal mixing downstream. Thus, increasing Re significantly enhances the convective heat transfer rate while reducing the overall temperature level near the cylinders.

The combined analysis of Figures 4.3–4.5 demonstrates that an increase in the Reynolds number strengthens inertial effects, intensifies microrotation, and enhances convective heat transfer. Consequently, higher Re leads to a more complex flow structure characterized by elongated wake zones, increased rotational motion, and reduced thermal boundary layer thickness.

4.5.4 Impacts of Micropolar Coupling Parameter

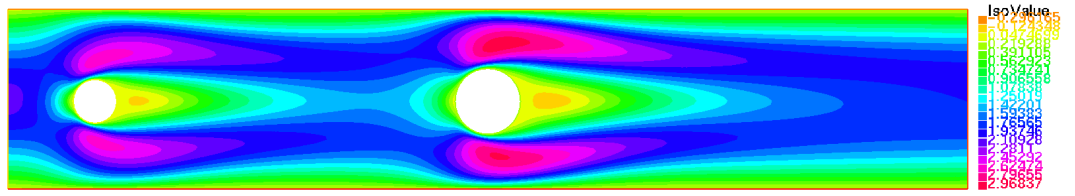

(a) $K = 0.01$

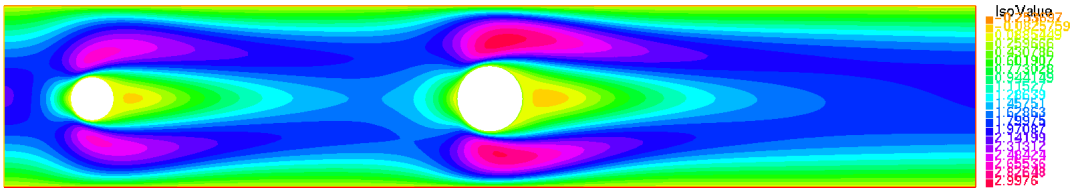

(b) $K = 0.1$

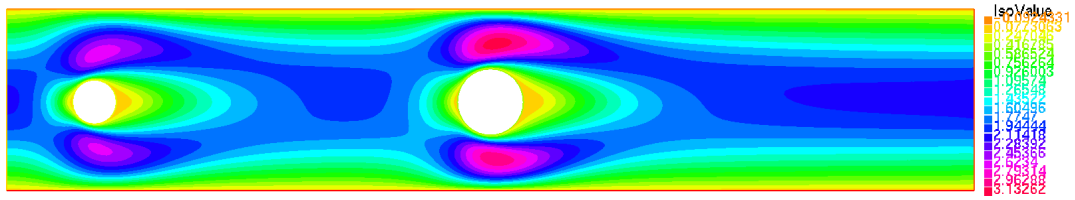

(c) $K = 1$

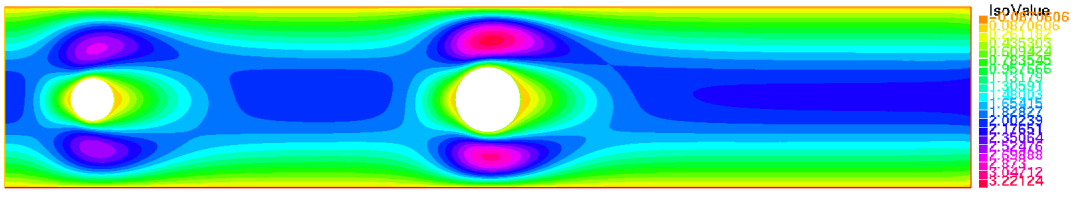

(d) $K = 3$

FIGURE 4.6: Contours of streamwise velocity U for different coupling parameter values ($K = 0.01$–3) at fixed $Re = 200$. Increasing K strengthens the coupling between microrotation and linear momentum, altering the recirculation structure and velocity gradients near the cylinders. Parameters: $Er = 0.1$, $Pr = 0.1$, $Ec = 0.1$, $Rd = 0.1$, $Ms = 0.1$, $\alpha = 1$, $\beta = 2$, $\Gamma = 0.5$.

Figures 4.6–4.8 illustrate the influence of the micropolar coupling parameter on the streamwise velocity, microrotation velocity, and temperature fields at a fixed Reynold number $Re = 200$. The coupling parameter K characterizes the interaction strength between the linear velocity field and the microrotation of fluid microelements. Physically, a higher K enhances the spin–velocity coupling, leading to a more complex transfer of angular momentum within the fluid.

In Figure 4.6, the contours of the streamwise velocity U are presented for $K = 0.01$, 0.1, 1, and 3. It is observed for small $K = 0.01$ (Figure 4.6(a)), the micropolar effects are negligible, and the flow behaves almost like a Newtonian fluid. The velocity distribution remains smooth, with a moderate recirculation region behind the downstream cylinder. When K increases to 0.1 (Figure 4.6(b)), coupling effects begin to appear, slightly modifying the velocity gradients near the cylinders. The recirculation zone behind the downstream cylinder becomes more compact, and the maximum velocity between the cylinders increases. For $K = 1$ (Figure 4.6(c)), the coupling between translational and rotational motion strengthens, resulting in a more pronounced reduction in the magnitude of U near the walls due to the transfer of linear momentum into microrotation energy. At $K = 3$ (Figure 4.6(d)), a significant alteration in flow structure occurs. The wake region behind the cylinders becomes elongated, indicating that stronger micropolar effects enhance fluid rotation and modify the effective viscosity of the medium. Overall, increasing K tends to suppress the primary flow velocity in the near-wall region while increasing vorticity in the wake, reflecting a redistribution of momentum between linear and angular motion.

Figure 4.7 shows the microrotation velocity W for the same range of K. It is seen that for $K = 0.01$ (Figure 4.7(a)), microrotation activity is weak and confined close to the solid boundaries, implying minimal spin motion of microelements. As K increases to 0.1 (Figure 4.7(b)), the microrotation magnitude intensifies near the cylinder surfaces and in the wake region, revealing stronger coupling between the microstructure and the macroscopic velocity field. At $K = 1$ and 3 (Figures 4.7(c) and 4.7(d)), microrotation zones expand significantly, especially in the recirculation region. This enhancement indicates that the micropolar fluid

exhibits a higher resistance to shear, accompanied by more pronounced spin effects. Hence, higher K amplifies the local angular momentum of microelements and redistributes energy between rotational and translational components of motion.

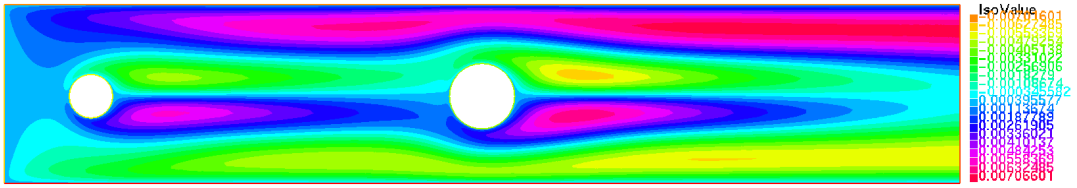

(a) $K = 0.01$

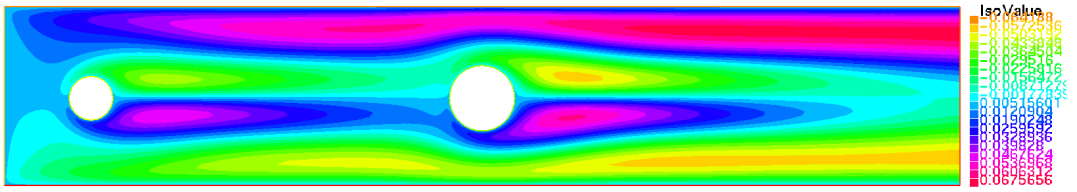

(b) $K = 0.1$

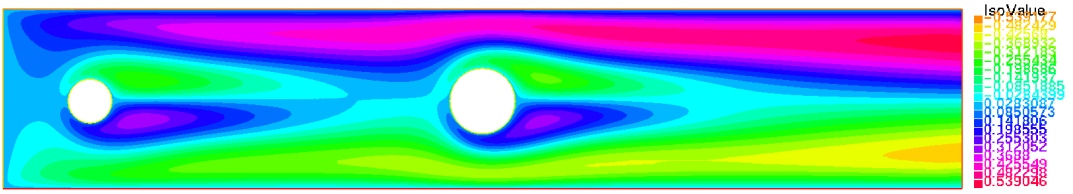

(c) $K = 1$

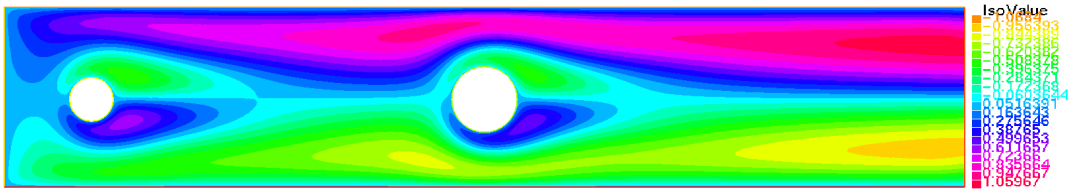

(d) $K = 3$

FIGURE 4.7: Contours of microrotation velocity W for different coupling parameter values ($K = 0.01$–3) at $Re = 200$. As K increases, microrotation intensity near the cylinder surfaces and in the wake region rises, indicating stronger particle rotation–velocity interaction. Parameters: $Er = 0.1$, $Pr = 0.1$, $Ec = 0.1$, $Rd = 0.1$, $Ms = 0.1$, $\alpha = 1$, $\beta = 2$, $\Gamma = 0.5$.

The temperature contours in Figure 4.8 depict the effect of K on the thermal field. It is seen that for low $K = 0.01$ (Figure 4.8(a)), the temperature distribution is nearly symmetric and dominated by conduction, with a thick thermal boundary layer near the cylinders.

As K increases to 0.1 and 1 (Figures 4.8(b) and 4.8(c)), the enhanced microrotation contributes to mild energy dissipation, leading to a slight increase in fluid

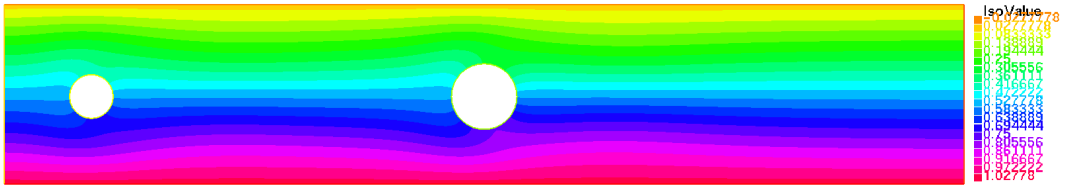

(a) $K = 0.01$

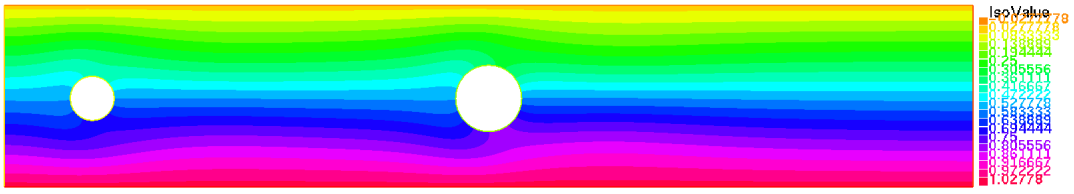

(b) $K = 0.1$

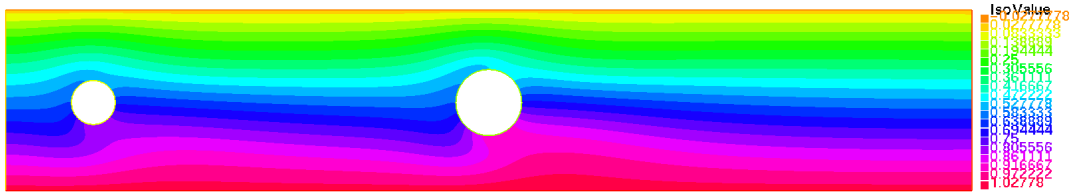

(c) $K = 1$

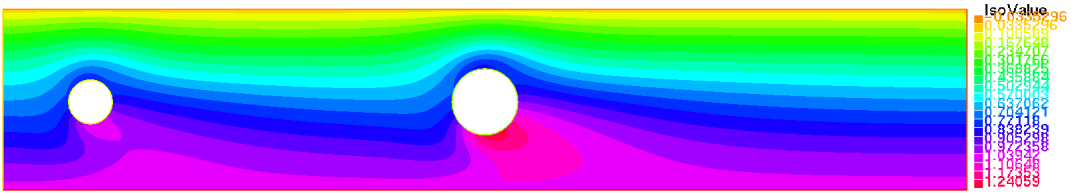

(d) $K = 3$

FIGURE 4.8: Temperature contours (θ) for different coupling parameter values ($K = 0.01$–3) at $Re = 200$. Increasing K slightly modifies the thermal boundary layer due to enhanced coupling effects between microrotation and translational flow. Parameters: $Er = 0.1$, $Pr = 0.1$, $Ec = 0.1$, $Rd = 0.1$, $Ms = 0.1$, $\alpha = 1$, $\beta = 2$, $\Gamma = 0.5$.

temperature near the solid surfaces and a thinner thermal boundary layer. For $K = 3$ (Figure 4.8(d)), the temperature contours become smoother and more aligned with the streamlines, signifying improved convective mixing and a moderate rise in local temperature near the downstream region. The results demonstrate that stronger micropolar coupling slightly augments thermal mixing due to intensified rotational motion of microelements, though the overall influence on temperature is less dominant than on velocity fields. In summary, increasing the coupling parameter K strengthens the rotational–translational interaction within the fluid, thereby increasing microrotation intensity, modifying the flow structure,

and slightly enhancing the convective heat transfer. These effects highlight the role of micropolarity in altering both hydrodynamic and thermal characteristics compared to classical Newtonian flow behavior.

4.5.5 Impacts of The Eringen Number

Figures 4.9–4.11 depict the influence of the Eringen number on the flow and thermal fields, including the streamwise velocity, microrotation velocity, and temperature, for fixed parameters ($Re = 300$, $K = 0.1$, $Pr = 0.1$, $Ec = 0.1$, $Rd = 0.1$, $Ms = 0.1$, $\alpha = 1$, $\beta = 2$, $\Gamma = 1$). The Eringen number is defined as $Er = j/D^2$, where j is the micro-inertia density and D is the cylinder diameter (characteristic length). This parameter represents the relative importance of micro-inertia effects compared to the macroscopic length scale. A higher Er indicates greater micro-inertia, which influences the angular momentum balance and the coupling between linear and rotational motions.

In Figure 4.9, the contours of the streamwise velocity U are shown for $Er = 0.005$, 0.01, 0.05, and 0.1. It is observed that for $Er = 0.005$ (Figure 4.9(a)), the velocity field is highly disturbed with extended recirculation zones behind both cylinders. The fluid exhibits strong rotational coupling, and the velocity gradients are sharper near the wall, indicating pronounced microstructural activity. Increasing Er to 0.01 (Figure 4.9(b)) reduces the strength of microrotational coupling, leading to smoother velocity contours and a slight reduction in wake size. The flow becomes more streamlined as the viscous contribution of microelements increases. At $Er = 0.05$ (Figure 4.9(c)), the recirculation zone behind the downstream cylinder further shrinks, and the high-velocity core between the cylinders becomes stronger. This demonstrates that an increase in Er suppresses microrotation-induced disturbances, allowing more stable flow development. For $Er = 0.1$ (Figure 4.9(d)), the velocity field attains near-symmetric structure with a shorter wake and reduced separation length, confirming that high Er values enhance the effective viscosity and stabilize the flow pattern. Overall, increasing the Eringen number weakens

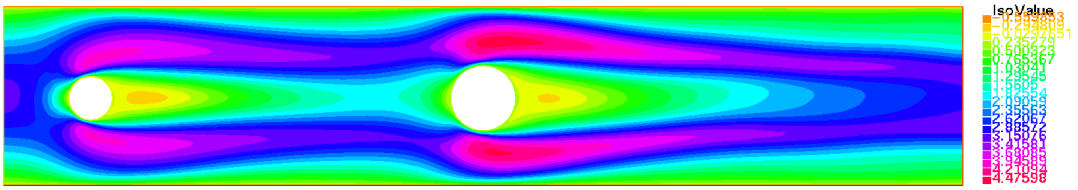

(a) $Er = 0.005$

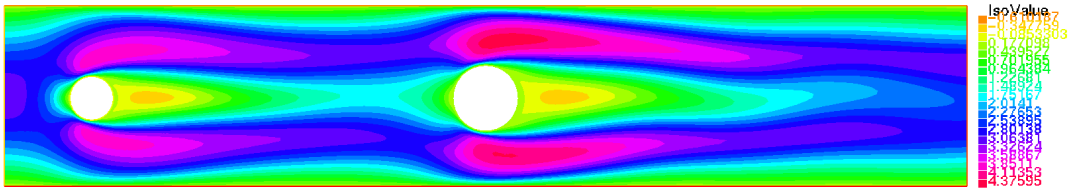

(b) $Er = 0.01$

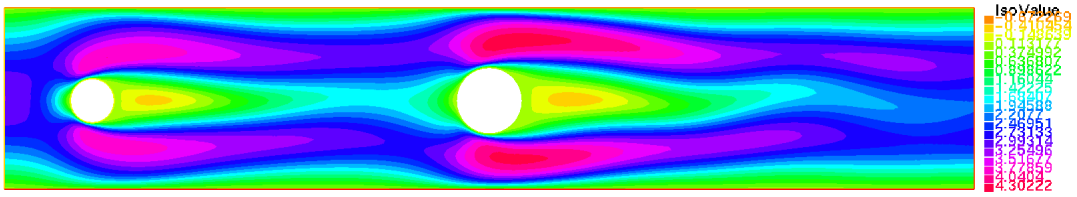

(c) $Er = 0.05$

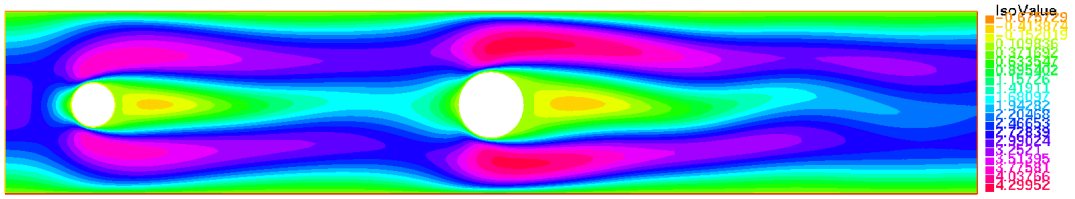

(d) $Er = 0.1$

FIGURE 4.9: Contours of streamwise velocity (U) for different Eringen numbers ($Er = 0.005$–0.1) at $Re = 300$, $K = 0.1$, $Pr = 0.1$, $Ec = 0.1$, $Rd = 0.1$, $Ms = 0.1$, $\alpha = 1$, $\beta = 2$, $\Gamma = 1$.

microrotation interactions, stabilizes the flow field, and suppresses secondary circulations.

Figure 4.10 illustrates the corresponding microrotation velocity W contours. It is seen that $Er = 0.005$ (Figure 4.10(a)), the microrotation intensity is high, especially near the cylinder surfaces and behind the downstream cylinder. The strong gradients indicate vigorous spinning of microelements due to low angular resistance. When Er increases to 0.01 (Figure 4.10(b)), the microrotation zone becomes more localized, and its magnitude decreases moderately. For $Er = 0.05$ (Figure 4.10(c)), the microrotation intensity further diminishes, showing that higher angular viscosity suppresses spin motion. The rotational activity is mostly

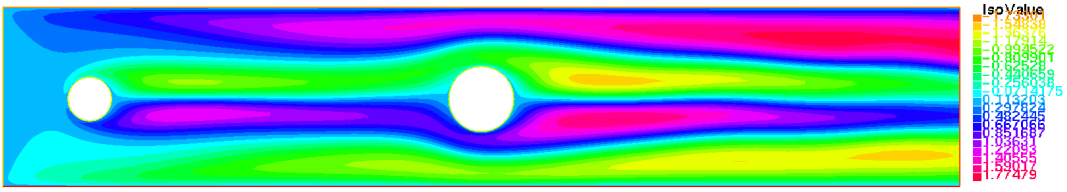

(a) $Er = 0.005$

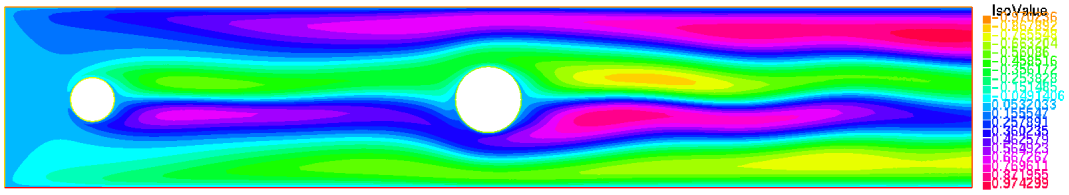

(b) $Er = 0.01$

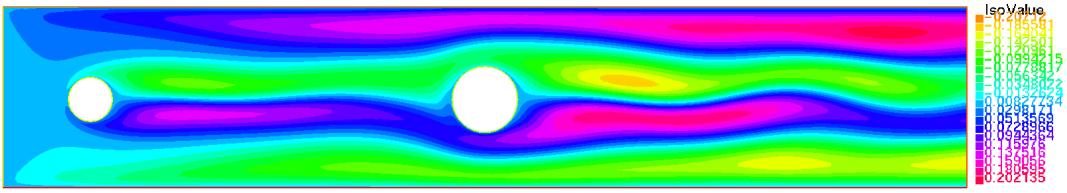

(c) $Er = 0.05$

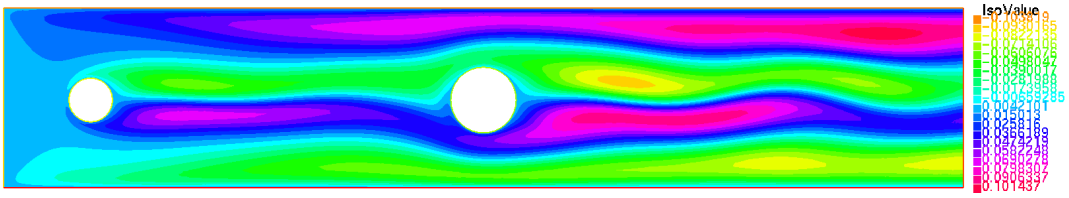

(d) $Er = 0.1$

FIGURE 4.10: Contours of microrotation velocity (W) for different Eringen numbers ($Er = 0.005$–0.1) at $Re = 300$, $K = 0.1$, $Pr = 0.1$, $Ec = 0.1$, $Rd = 0.1$, $Ms = 0.1$, $\alpha = 1$, $\beta = 2$, $\Gamma = 1$.

confined near the walls. At $Er = 0.1$ (Figure 4.10(d)), the microrotation effects are minimal, and the contours appear smoother with nearly uniform gradients, suggesting a transition toward Newtonian-like behavior. This analysis confirms that larger Er values restrict microrotational motion by enhancing angular viscous resistance, thereby reducing the local spin energy and stabilizing the microstructure of the fluid. The temperature distributions for the same range of values are shown in Figure 4.11. It is observed that for small $Er = 0.005$ (Figure 4.11(a)), the temperature field exhibits a wider spread and higher temperature levels due to strong micro-rotation activity, which promotes energy dispersion and localized heating.

As Er increases to 0.01 (Figure 4.11(b)), the temperature contours become more

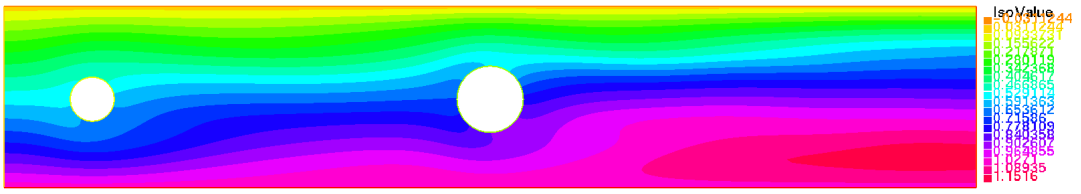

(a) $Er = 0.005$

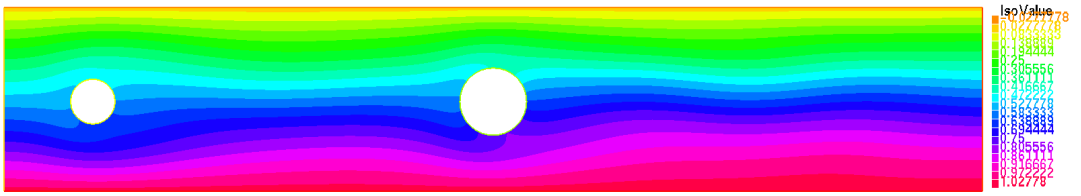

(b) $Er = 0.01$

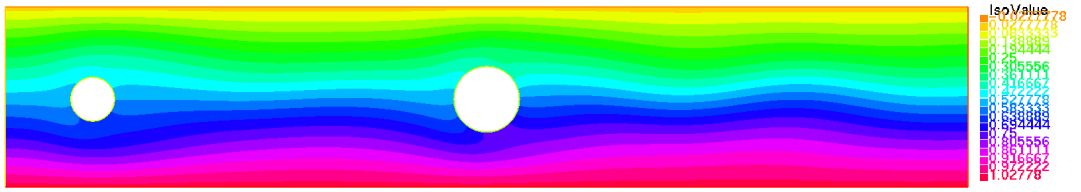

(c) $Er = 0.05$

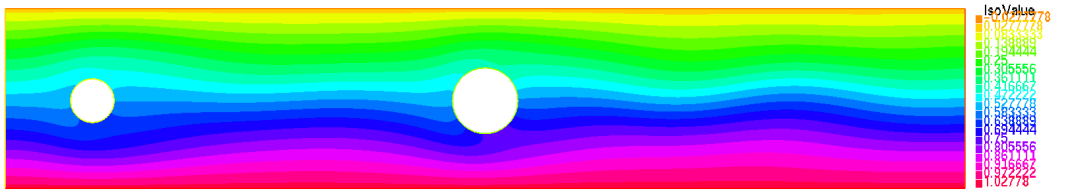

(d) $Er = 0.1$

FIGURE 4.11: Contours of temperature (θ) for different Eringen numbers ($Er =$ 0.005–0.1) at $Re = 300$, $K = 0.1$, $Pr = 0.1$, $Ec = 0.1$, $Rd = 0.1$, $Ms = 0.1$, $\alpha = 1$, $\beta = 2$, $\Gamma = 1$.

compact, and the overall temperature magnitude decreases slightly, indicating that weaker microrotation leads to reduced internal energy generation. At $Er = 0.05$ (Figure 4.11(c)), the temperature gradients near the cylinder surfaces become steeper, while the temperature downstream decreases, showing enhanced convective cooling. For $Er = 0.1$ (Figure 4.11(d)), the temperature distribution becomes uniform with thinner thermal boundary layers, representing more efficient convective heat transport and reduced microrotational dissipation. Therefore, as the Eringen number increases, the influence of microrotation on heat generation weakens, leading to cooler and more stable temperature profiles. In summary, the increase in the Eringen number (Er) leads to suppression of microrotation effects,

smoother velocity and temperature fields, and reduced thermal disturbances. Low Er values correspond to fluids with active micro-rotational dynamics, exhibiting stronger coupling and higher internal energy generation. Conversely, high Er values enhance angular viscosity, stabilize the flow, and improve the efficiency of convective heat transfer in micropolar magneto-thermal systems.

4.5.6 Impacts of Prandtl Number

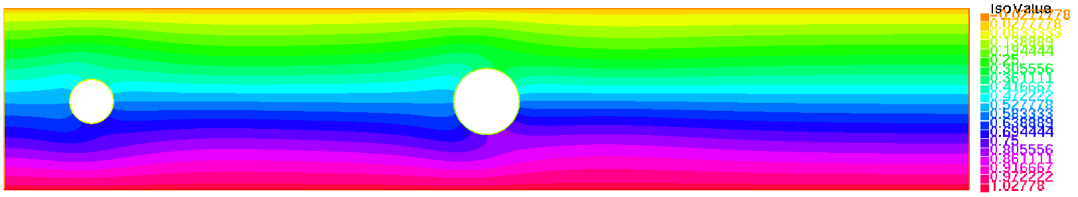

(a) $Pr = 0.1$

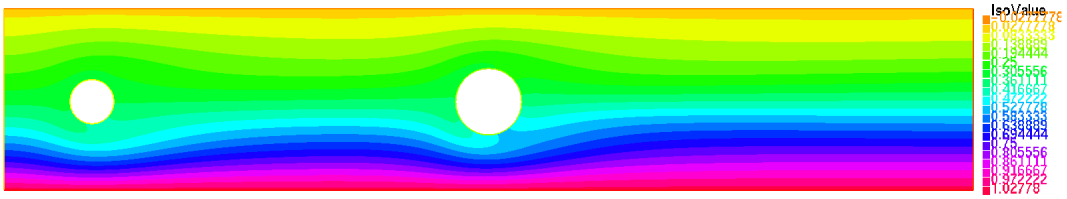

(b) $Pr = 0.5$

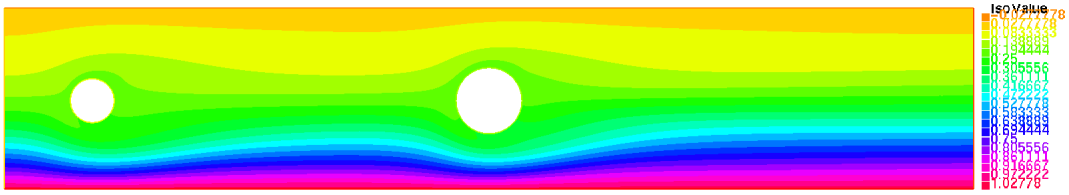

(c) $Pr = 1$

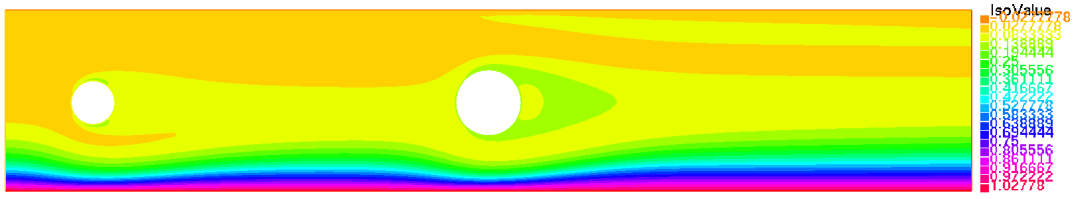

(d) $Pr = 5$

FIGURE 4.12: Contours of temperature (θ) for different Prandtl numbers ($Pr = 0.1$–5) at $Re = 200$, $K = 0.1$, $Er = 0.1$, $Ec = 0.1$, $Rd = 0.1$, $Ms = 0.1$, $\alpha = 1$, $\beta = 2$, $\Gamma = 0.5$.

Figure 4.12 illustrates the effect of the Prandtl number on the temperature distribution θ at a fixed Reynolds number $Re = 200$. The Prandtl number quantifies the

ratio of momentum diffusivity to thermal diffusivity and hence controls the relative thickness of the velocity and thermal boundary layers. Fluids with low Pr possess high thermal diffusivity (such as liquid metals), while those with high Pr (such as oils) exhibit thicker velocity layers but thinner thermal layers. As observed in Figure 4.12(a), for a low Prandtl number ($Pr = 0.1$), the temperature field is smooth and widely spread, showing a thick thermal boundary layer around both cylinders. The high thermal diffusivity in this case promotes strong heat conduction, leading to a more uniform temperature distribution within the domain. When Pr increases to 0.5 (Figure 4.12(b)), the temperature gradients near the solid surfaces become steeper, and the thermal boundary layer thickness decreases.This indicates a shift from conduction-dominated to convection-dominated heat transfer. The downstream region shows cooler fluid zones, suggesting that heat is transported away more effectively by advection. At $Pr = 1$ (Figure 4.12(c)), the balance between momentum and heat diffusion leads to clearly defined thermal layers around the cylinders.

The temperature contours become more compressed near the wall, and convective transport becomes stronger, showing higher temperature gradients and reduced near-wall temperature levels. For a high Prandtl number ($Pr = 5$, Figure 4.12(d)), the temperature boundary layer becomes very thin and closely follows the velocity boundary layer. The temperature field shows sharper gradients and reduced diffusion, meaning that the fluid's ability to conduct heat decreases while convection dominates the overall energy transport. Overall, increasing the Prandtl number results in a thinner thermal boundary layer, stronger temperature gradients, and enhanced convective heat transfer rates. This trend is consistent with classical heat transfer theory, confirming that higher Pr values suppress thermal diffusion and intensify the convective transport process in micropolar fluids under the influence of magnetic and rotational effects.

These observations confirm that Pr plays a crucial role in determining the thermal boundary layer structure and overall heat transfer performance. The next subsection examines the additional influence of viscous dissipation, characterized by the Eckert number, on the temperature field.

4.5.7 Impacts of Eckert Number

Figure 4.13 illustrates the effect of the Eckert number (Ec) on the temperature field θ for fixed parameters ($Re = 200$, $K = 0.1$, $Er = 0.1$, $Pr = 0.1$, $Rd = 0.1$, $Ms = 0.1$, $\alpha = 1$, $\beta = 2$, $\Gamma = 0.5$). The Eckert number represents the ratio of kinetic energy to enthalpy difference and quantifies the influence of viscous dissipation on the thermal field. A higher Ec implies stronger conversion of mechanical energy into internal energy, leading to additional heating within the flow domain.

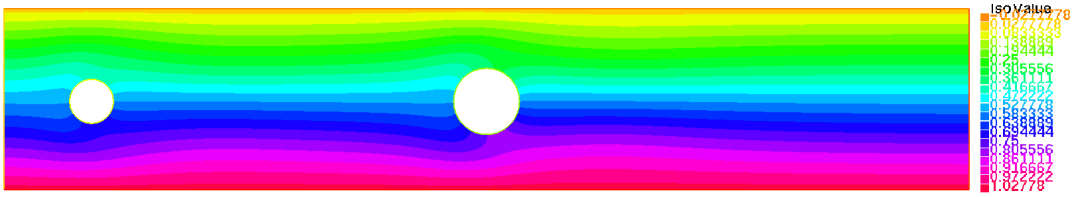

(a) $Ec = 0.1$

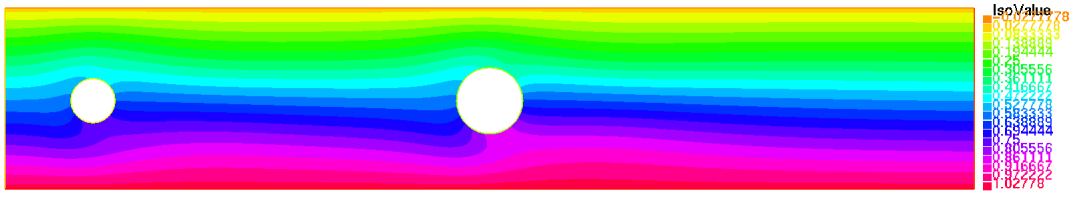

(b) $Ec = 0.5$

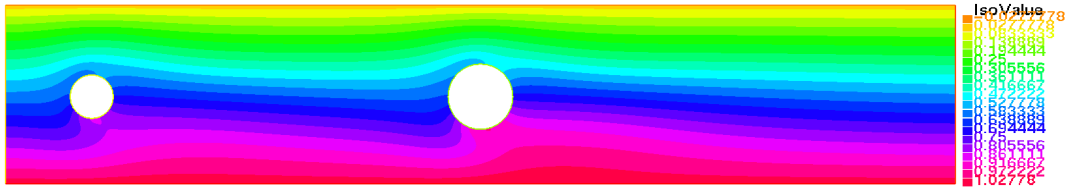

(c) $Ec = 1$

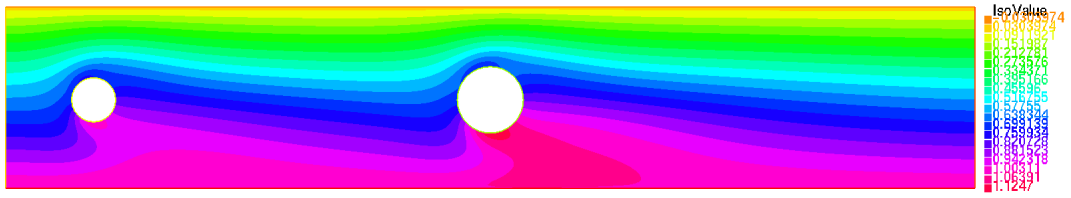

(d) $Ec = 2$

FIGURE 4.13: Contours of temperature (θ) for different Eckert numbers ($Ec = 0.1$–2) at $Re = 200$, $K = 0.1$, $Er = 0.1$, $Pr = 0.1$, $Rd = 0.1$, $Ms = 0.1$, $\alpha = 1$, $\beta = 2$, $\Gamma = 0.5$.

At the lowest Eckert number ($Ec = 0.1$, Figure 4.13(a)), the temperature field remains relatively uniform, and the thermal boundary layer is thin. The viscous

dissipation effect is minimal, resulting in lower fluid temperatures and negligible internal heat generation. Heat transfer in this regime is primarily due to conduction and convection mechanisms. When Ec increases to 0.5 (Figure 4.13(b)), a noticeable rise in fluid temperature is observed near the cylinder surfaces and in the wake region. The viscous heating effect becomes more apparent, especially in regions of high velocity gradients. Consequently, the temperature contours expand outward, and the temperature gradients near the solid boundaries become steeper. At $Ec = 1$ (Figure 4.13(c)), the contribution of viscous dissipation to the thermal energy balance becomes significant. The temperature levels throughout the flow field increase, with stronger heating near the reattachment zone and downstream of the cylinders. The thermal boundary layer thickens slightly due to enhanced energy diffusion, and convective heat transfer becomes dominant. For the highest Eckert number ($Ec = 2$, Figure 4.13(d)), the entire fluid domain experiences a substantial temperature rise. The regions near the cylinders exhibit intense local heating caused by strong shear layers and high viscous dissipation rates. The temperature contours appear denser and more elongated in the streamwise direction, indicating the accumulation of internal energy in the flow. In summary, increasing the Eckert number intensifies viscous dissipation effects, leading to elevated temperature levels and thicker thermal boundary layers. The results confirm that higher Ec values significantly enhance internal heat generation within the micropolar fluid, thereby influencing both the thermal structure and the overall heat transfer behavior. This effect is particularly relevant in high-speed or high-viscosity micropolar flows, where mechanical energy is efficiently converted into thermal energy.

4.5.8 Impacts of Radiation Parameter

Figure 4.14 illustrates the influence of the radiation parameter on the temperature field θ for a fixed set of flow parameters ($Re = 200$, $K = 0.1$, $Er = 0.1$, $Pr = 0.1$, $Ec = 0.1$, $Ms = 0.1$, $\alpha = 1$, $\beta = 2$, $\Gamma = 0.5$). The radiation parameter measures the relative contribution of thermal radiation to conductive heat transfer. A higher

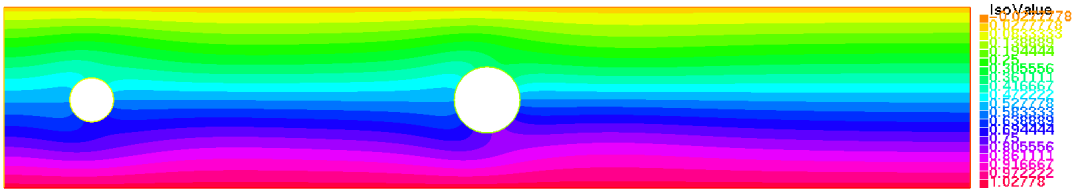

(a) $Rd = 0.1$

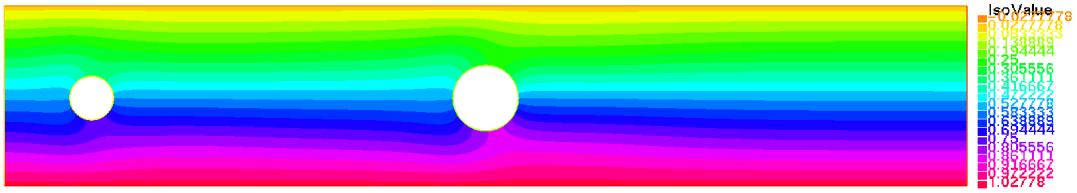

(b) $Rd = 0.5$

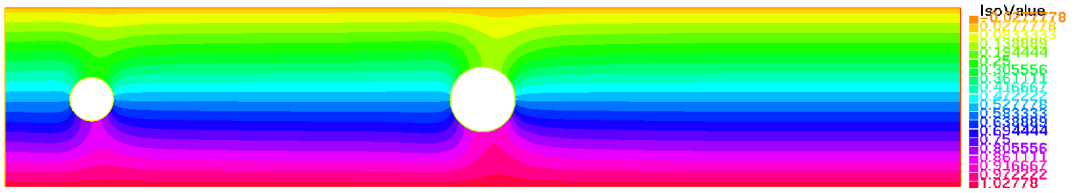

(c) $Rd = 1$

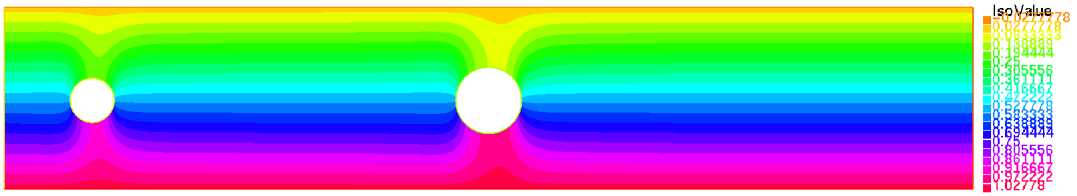

(d) $Rd = 5$

FIGURE 4.14: Contours of temperature (θ) for different radiation parameters ($Rd = 0.1$–5) at $Re = 200$, $K = 0.1$, $Er = 0.1$, $Pr = 0.1$, $Ec = 0.1$, $Ms = 0.1$, $\alpha = 1$, $\beta = 2$, $\Gamma = 0.5$.

Rd corresponds to stronger radiative heat flux within the fluid domain, which can significantly affect the overall temperature distribution.

At the lowest radiation parameter ($Rd = 0.1$, Figure 4.14(a)), the temperature field exhibits low intensity and a thick thermal boundary layer around both cylinders. The dominance of conductive heat transfer results in a relatively uniform temperature distribution with minimal radiative effects. As Rd increases to 0.5 (Figure 4.14(b)), noticeable changes appear in the thermal field. The temperature gradients near the cylinder surfaces become steeper, and the downstream region shows elevated temperature levels. This indicates that radiative heating begins to play a significant role, enhancing energy transport from the high-temperature

regions toward the cooler flow areas. For $Rd = 1$ (Figure 4.14(c)), the influence of radiation becomes more pronounced. The temperature contours spread farther into the fluid region, demonstrating enhanced energy diffusion through radiation. The thermal boundary layer becomes slightly thicker, while the overall temperature level in the domain rises. At the highest radiation parameter ($Rd = 5$, Figure 4.14(d)), the entire flow field shows a substantial increase in temperature magnitude. The thermal boundary layer expands further, and the contours exhibit smoother transitions due to strong radiative heat transfer dominating over conduction. Consequently, the effect of radiation leads to a reduction in temperature gradients near the solid surfaces but an overall increase in mean fluid temperature. In summary, increasing the radiation parameter Rd intensifies the radiative energy transport, leading to higher temperature levels throughout the domain and thicker thermal boundary layers. This trend highlights the crucial role of radiative heat transfer in micropolar fluid flows, especially in thermally sensitive systems where radiation significantly modifies the heat distribution and overall thermal performance.

4.5.9 Impacts of Magnetization Parameter

Figure 4.15 presents the influence of the magnetization dissipation parameter on the temperature field at fixed flow parameters ($Re = 200$, $K = 0.1$, $Er = 0.1$, $Pr = 0.1$, $Ec = 0.1$, $Rd = 0.1$, $Ms = 1$, $\alpha = 1$, $\beta = 2$). The parameter Γ characterizes the relative contribution of magnetic dissipation effects to the overall energy balance. It quantifies the conversion of magnetic energy into thermal energy through magnetization relaxation processes, thereby influencing the internal heating and temperature distribution within the magneto-micropolar fluid. At the lowest value $\Gamma = 0.1$ (Figure 4.15(a)), the magnetic dissipation effects are minimal, resulting in a thin thermal boundary layer around the cylinders. The temperature field exhibits low intensity and nearly uniform gradients, indicating that magnetization-induced heating has negligible influence on heat transfer at small Γ values. The thermal patterns are primarily governed by convective and conductive

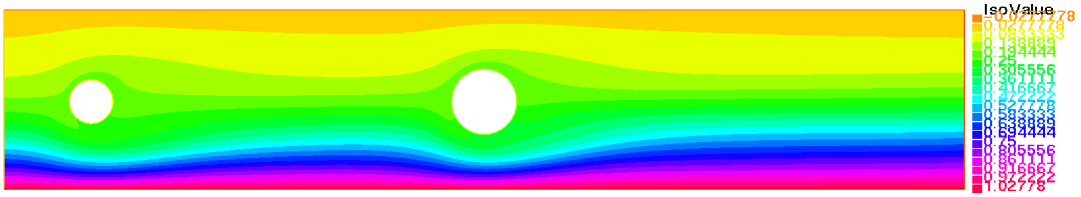

(a) $\Gamma = 0.1$

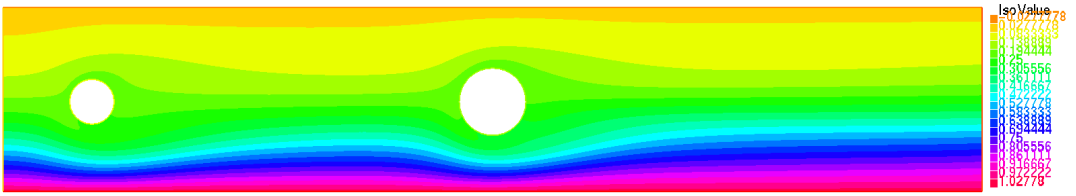

(b) $\Gamma = 0.5$

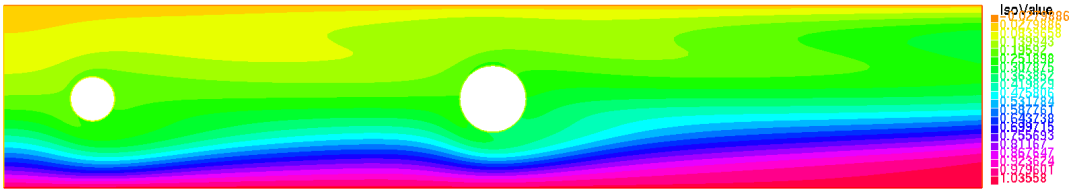

(c) $\Gamma = 1$

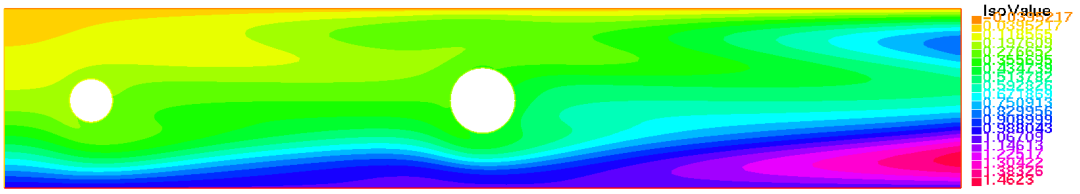

(d) $\Gamma = 3$

FIGURE 4.15: Contours of temperature (θ) for different magnetization dissipation parameters ($\Gamma = 0.1$–3) at $Re = 200$, $K = 0.1$, $Er = 0.1$, $Pr = 0.1$, $Ec = 0.1$, $Rd = 0.1$, $Ms = 1$, $\alpha = 1$, $\beta = 2$.

mechanisms. When Γ increases to 0.5 (Figure 4.15(b)), magnetic dissipation becomes more significant, leading to moderate internal heating within the fluid. The temperature contours show slight expansion near the downstream region, indicating enhanced energy conversion from magnetic to thermal forms. The thermal boundary layer thickens moderately, and temperature levels rise in the wake region due to increased magnetic energy dissipation. At $\Gamma = 1$ (Figure 4.15(c)), the effect of magnetization dissipation becomes prominent. The magnetic energy is more effectively converted into thermal energy throughout the fluid domain, which elevates the overall temperature field. The temperature gradients near the walls become smoother, and the flow demonstrates improved thermal uniformity across

the domain due to distributed magnetic heating. For the highest case $\Gamma = 3$ (Figure 4.15(d)), the temperature field exhibits significantly expanded heated regions with more uniform contours around both cylinders. The thermal boundary layer becomes substantially thicker, and local temperatures near cylinder surfaces increase noticeably. This behavior arises because higher Γ values enhance magnetic dissipation rates, resulting in additional energy conversion into heat through magnetization relaxation processes. In summary, an increase in Γ enhances magnetic dissipation within the magneto-micropolar fluid, leading to elevated temperature levels and thicker thermal boundary layers. The stronger magnetization dissipation improves internal energy generation, indicating that Γ plays a crucial role in controlling the thermal response and heat transfer characteristics in magneto-micropolar convective flows through magnetic energy conversion mechanisms.

Chapter 5

Conclusion

In this thesis a comprehensive numerical investigation of radiative magneto micropolar flow and heat transfer in a channel containing dual cylinders arranged in tandem configuration is carried out. The study successfully developed and validated a computational framework capable of handling the complex multiphysics coupling between microrotational effects, magnetic fields, and thermal radiation. Building upon the established Turek and Schafer benchmark case, the research extended the analysis to incorporate Eringen's micropolar theory combined with magnetohydrodynamics and radiative heat transfer. The mathematical formulation incorporated the complete set of governing equations for mass, linear momentum, angular momentum, and energy conservation, along with appropriate boundary conditions for the dual-cylinder configuration. The finite element method with Taylor-Hood (P_2-P_1) elements was employed for spatial discretization, while the backward Euler scheme was used for temporal discretization. The weak formulation and solution algorithm ensured stable and accurate simulations of the coupled phenomena.

The parametric study conducted in this research thesis has yielded several significant insights into the behavior of radiative magneto-micropolar flows in complex geometries. The Reynolds number exhibited a profound influence on the flow characteristics and heat transfer performance.

As Re increased from 100 to 400, enhanced flow separation and more pronounced recirculation zones were observed in the wake region. The stronger inertial effects at higher Reynolds numbers intensified the microrotation activity, leading to increased microstructural interactions within the fluid. Simultaneously, the thermal boundary layer thickness was reduced, resulting in improved convective heat transfer. Moreover, the flow field exhibited increasingly complex vortex dynamics and wake interference patterns, indicating the development of more intricate flow behavior. The micropolar coupling parameter and the Eringen number significantly influenced both the hydrodynamic and thermal behavior of the flow. Higher values of K strengthened the coupling between translational and rotational motions, leading to noticeable modifications in velocity gradients and recirculation patterns. An increase in K also enhanced the intensity of microrotation, particularly near solid boundaries and within wake regions. Conversely, lower values of Er promoted stronger microrotational activity and increased internal energy generation within the fluid. In contrast, higher Er values contributed to the stabilization of the flow field and effectively suppressed microrotation effects. The magnetic parameters and thermal radiation played crucial roles in flow control and heat transfer enhancement. The presence of a magnetic field effectively suppressed vortex shedding and significantly modified the wake dynamics. Thermal radiation led to a notable elevation in temperature levels throughout the computational domain, highlighting its importance in high-temperature flow regimes. The radiation parameter (Rd) governed the relative contribution of radiative heat transfer compared to conductive heat transfer. In addition, viscous dissipation effects, characterized by the Eckert number (Ec), contributed substantially to internal heat generation within the fluid. The combined effects of micropolar, magnetic, and radiation parameters revealed optimal conditions for heat transfer enhancement. Higher Reynolds and Prandtl numbers promoted convective dominance within the flow, while moderate values of the micropolar coupling parameter (K) and the Eringen number (Er) yielded optimal thermal-hydraulic performance. Radiation effects became particularly significant in high-temperature applications, influencing the overall temperature distribution. Furthermore, the magnetization

dissipation parameter (Γ) played a important role in shaping the thermal boundary layer and determining the energy distribution throughout the domain. Based on the findings of this study, the following research directions are recommended:

i) Extension to three-dimensional simulations to capture complex vortex structures and secondary flows.

ii) Investigation of temperature-dependent viscosity and thermal conductivity effects.

iii) Application of machine learning techniques for optimization and control of such complex flows.

iv) Exploration of different cylinder arrangements (staggered, triangular) and their effects on thermal-hydraulic performance.

This research has successfully developed a comprehensive computational framework for analyzing radiative magneto-micropolar flows in complex geometries. The systematic parametric studies have provided fundamental insights into the coupled effects of Eringen's micropolar parameters, magnetic fields, and thermal radiation on flow characteristics and heat transfer performance. The findings contribute to the fundamental understanding of complex multiphysics flows and provide practical guidelines for designing advanced thermal management systems in various engineering applications, including heat exchangers, microfluidic devices, and electronic cooling systems.

Bibliography

[1] M. Zdravkovich, *"Flow around circular cylinders: Volume 2: Applications"*. Oxford university press, 1997, vol. 2.

[2] A. Eringen, "Theory of micropolar fluids," *Journal of Mathematics and Mechanics*, vol. 16, no. 1, pp. 1–18, 1966.

[3] G. Lukaszewicz, *"Micropolar fluids: theory and applications"*. Birkhäuser, 1999.

[4] G. Sutton and A. Sherman, *"Engineering magnetohydrodynamics"*. Courier Dover Publications, 2006.

[5] R. Moreau, *"Magnetohydrodynamics"*. Springer Science & Business Media, 2013, vol. 3.

[6] T. Igarashi, "Characteristics of the flow around two circular cylinders arranged in tandem: 1st report," *Bulletin of JSME*, vol. 24, no. 188, pp. 323–331, 1981.

[7] Igarashi, "Characteristics of the flow around two circular cylinders arranged in tandem: 2nd report, unique phenomenon at small spacing," *Bulletin of JSME*, vol. 27, no. 233, pp. 2380–2387, 1984.

[8] A. Eringen, *"Microcontinuum Field Theories: II. Fluent Media"*. Springer-Verlag, 2001.

[9] T. Ariman, M. Turk, and N. Sylvester, "Review article: Microcontinuum fluid mechanics—a review," *International Journal of Engineering Science*, vol. 11, no. 8, pp. 905–930, 1973.

[10] D. Rees and A. Bassom, "The blasius boundary-layer flow of a micropolar fluid," *International Journal of Engineering Science*, vol. 34, no. 1, pp. 113–124, 1996.

[11] I. Papautsky, J. Brazzle, T. Ameel, and A. Frazier, "Laminar fluid behavior in microchannels using micropolar fluid theory," *Sensors and actuators A: Physical*, vol. 73, no. 1-2, pp. 101–108, 1999.

[12] R. Mohamed and S. Abo-Dahab, "Influence of chemical reaction and thermal radiation on the heat and mass transfer in mhd micropolar flow over a vertical moving porous plate in a porous medium with heat generation," *International Journal of Thermal Sciences*, vol. 48, no. 9, pp. 1800–1813, 2009.

[13] G. Shit and M. Roy, "Transient mhd flow and heat transfer of micropolar fluid in a channel," *International Journal of Engineering Science*, vol. 49, no. 10, pp. 1051–1061, 2011.

[14] I. K. M. S. Khan, M.A. Memon and S. Eldin, "Finite element based direct and iterative approach to investigate a magneto-micropolar flow through a rectangular channel," *Alexandria Engineering Journal*, vol. 75, pp. 55–66, 2023.

[15] H. Alfvén, "Existence of electromagnetic-hydrodynamic waves," *Nature*, vol. 150, no. 3805, pp. 405–406, 1942.

[16] D. Chatterjee and S. Gupta, "Mhd flow and heat transfer behind a square cylinder in a duct under strong axial magnetic field," *International Journal of Heat and Mass Transfer*, vol. 88, pp. 1–13, 2015.

[17] J. Maurya, S. Yadav, and A. Singh, "Magnetohydrodynamic transient flow in a circular cylinder," *International Journal of Dynamics and Control*, vol. 6, no. 4, pp. 1477–1483, 2018.

[18] B. Carmo and J. Meneghini, "Numerical investigation of the flow around two circular cylinders in tandem," *Journal of Fluids and Structures*, vol. 22, no. 6-7, pp. 979–988, 2006.

[19] U. Ali, M. Islam, I. Janajreh, Y. Fatt, and M. Alam, "Hydrodynamic and thermal behavior of tandem, staggered, and side-by-side dual cylinders," *Physics of Fluids*, vol. 36, no. 1, 2024.

[20] V. Duong, V. Nguyen, V. Nguyen, P. Palar, L. Zuhal, T. Ngo, C. Dinh, and W. Wang, "A numerical study on dynamic flows past three tandem inclined elliptic cylinders near moving wall," *Physics of Fluids*, vol. 36, no. 2, 2024.

[21] M. Schäfer, S. Turek, F. Durst, E. Krause, and R. Rannacher, "Benchmark computations of laminar flow around a cylinder," in *Flow simulation with high-performance computers II: DFG priority research programme results 1993–1995*. Springer, 1996, pp. 547–566.

[22] J. Reddy, *"An Introduction to the Finite Element Method"*, 4th ed. McGraw-Hill, 2019.

[23] F. Hecht, "New development in freefem++," *Journal of Numerical Mathematics*, vol. 20, no. 3-4, pp. 251–265, 2012.

[24] G. Batchelor, *"An introduction to fluid dynamics"*. Cambridge university press, 2000.

[25] F. White and J. Majdalani, *"Viscous fluid flow"*. McGraw-Hill New York, 2006, vol. 3.

[26] R. Aris, *"Vectors, tensors and the basic equations of fluid mechanics"*. Courier Corporation, 2012.

[27] University of Cambridge, "Differential and integral approach," 2025, accessed: 2025-03-04. [Online]. Available: https://www-mdp.eng.cam.ac.uk/web/library/enginfo/aerothermal_dvd_only/aero/fprops/cvanalysis/node11.html

[28] R. Panton, *"Incompressible Flow"*, 4th ed. John Wiley & Sons, 2013.

[29] M. Gurtin, *"An Introduction to Continuum Mechanics"*, ser. Mathematics in Science and Engineering. Academic Press, 1982.

[30] A. Bejan, *"Convection Heat Transfer"*, 4th ed. John Wiley & Sons, 2013.

[31] P. Kundu, I. Cohen, and D. Dowling, *"Fluid Mechanics"*, 5th ed. Academic Press, 2012.

[32] G. Sofiadis, A. Liakopoulos, A. Palasis, and F. Sofos, "Turbulent micropolar open-channel flow," *Fluids*, vol. 9, no. 9, p. 202, 2024.

[33] P. M. Thakur and G. Hazarika, "Effects of variable viscosity and thermal conductivity on the mhd flow of micropolar fluid past an accelerated infinite vertical insulated plate," *International Journal of Heat and Technology*, vol. 33, no. 3, pp. 73–78, 2015.

[34] M. Khan, M. Bilal, N. Hajano, and F. Ixtiyarov, "Numerical investigation of eringen number effects on magneto–micropolar channel flow with a cuboid obstacle using freefem++," *Journal of Taibah University for Science*, vol. 20, no. 1, p. 2620319, 2026.

[35] J. Jackson, *"Classical Electrodynamics"*, 3rd ed. John Wiley & Sons, 1999.

[36] D. Griffiths, *"Introduction to Electrodynamics"*, 4th ed. Cambridge University Press, 2017.

[37] J. Shercliff, *"A Textbook of Magnetohydrodynamics"*. Pergamon Press, 1965.

[38] J. Howell, M. Mengüç, K. Daun, and R. Siegel, *"Thermal radiation heat transfer"*. CRC press, 2020.

[39] M. S. Khan, "A new thermal boundary layer analysis model in the presence of micromagnetorotation within micropolar continuum," *Multiscale and Multidisciplinary Modeling, Experiments and Design*, vol. 8, p. 387, 2025.